

Garrett M. Clayton

Department of Mechanical Engineering,
Villanova University,
Villanova, PA 19085
e-mail: garrett.clayton@villanova.edu

Szuchi Tien

Department of Mechanical Engineering,
National Cheng Kung University,
Tainan 701, Taiwan
e-mail: sctien@mail.ncku.edu.tw

Kam K. Leang

Department of Mechanical Engineering,
University of Nevada,
Reno, NV 89557
e-mail: kam@unr.edu

Qingze Zou

Department of Mechanical Engineering,
Iowa State University,
Ames, IA 50011
e-mail: qzzou@iastate.edu

Santosh Devasia¹

Department of Mechanical Engineering,
University of Washington,
Seattle, WA 98195
e-mail: devasia@u.washington.edu

A Review of Feedforward Control Approaches in Nanopositioning for High-Speed SPM

Control can enable high-bandwidth nanopositioning needed to increase the operating speed of scanning probe microscopes (SPMs). High-speed SPMs can substantially impact the throughput of a wide range of emerging nanosciences and nanotechnologies. In particular, inversion-based control can find the feedforward input needed to account for the positioning dynamics and, thus, achieve the required precision and bandwidth. This article reviews inversion-based feedforward approaches used for high-speed SPMs such as optimal inversion that accounts for model uncertainty and inversion-based iterative control for repetitive applications. The article establishes connections to other existing methods such as zero-phase-error-tracking feedforward and robust feedforward. Additionally, the article reviews the use of feedforward in emerging applications such as SPM-based nanoscale combinatorial-science studies, image-based control for subnanometer-scale studies, and imaging of large soft biosamples with SPMs.

[DOI: 10.1115/1.4000158]

1 Introduction

Control is critical for achieving high-bandwidth nanopositioning to increase the operating speed of scanning probe microscopes (SPMs), such as scanning tunneling microscopes (STMs) [1] and atomic force microscopes (AFMs) [2]. Increasing the operating speed of SPMs can significantly impact the throughput of a wide range of emerging nanosciences and nanotechnologies because SPMs are key enabling tools in the experimental investigation and manipulation of nanoscale biological, chemical, material, and physical processes; e.g., see Refs. [3–7]. A critical problem in high-speed SPM operation is to position the SPM-probe precisely over the sample surface. Positioning errors between the SPM-probe and sample surface can lead to damage of the sample and/or the probe, as well as introduce unwanted modification of the surface properties. To avoid the positioning problem at high operating speeds (induced by mechanical vibration), commercial SPMs typically operate at low speeds; for example, high-resolution SPMs scan the sample at around 1/100 to 1/10 of the lowest resonant-vibrational frequency. This positioning-related limitation to SPM operating speed motivates the development of control techniques that enable high-bandwidth nanopositioning in SPMs.

This article reviews the role of feedforward control in the development of high-speed SPMs. While the SPM probe-to-sample distance could be controlled using feedback methods, early SPMs did not have sensors to measure the scanning motion of the SPM-probe over the sample surface. Therefore, precision scanning of the probe over the sample surface relied on feedforward control methods. For example, the inputs to the SPM-probe positioner

(usually, a piezoelectric actuator) would be cycled to reset hysteresis-memory effects and thereby achieve repeatable positioning. Such resetting of memory effects for SPM control is discussed in Refs. [8,9]. The advent of SPMs with sensors for measuring the probe's scanning motion [10] has substantially improved the SPM performance through the use of modern feedback methods [11]. The addition of feedforward control to these feedback schemes enables even further performance improvement in SPMs [12] by overcoming limitations imposed by the need to balance (a) high-bandwidth precision positioning with (b) robust closed-loop stability in the presence of unmodeled dynamics and uncertainties. This article reviews recent efforts in feedforward control to increase the operating speed of SPMs.

The article begins with a brief review of SPM operation and the need for high-speed SPM to clarify the positioning issues in Sec. 2. Then, Sec. 3 discusses the limits on SPM operating speed due to vibration-caused positioning errors. Section 4 reviews feedforward control methods for high-speed SPM along with current research and implementation issues. While this article does not focus on SPM feedback control, it discusses the integration of feedforward with sensor-based feedback (in Sec. 4), as well as an image-based approach to feedforward control when sensors for feedback are not available (in Sec. 5). Additionally, Sec. 5 presents emerging applications where SPM feedforward control plays an important role: (a) SPM-based nanoscale combinatorial-science studies and (b) imaging of large soft samples with SPMs. A summary of the discussions and concluding remarks is provided in Sec. 6.

2 The Need for High-Bandwidth Nanopositioning

This section begins with a brief review of SPM operation to clarify the need for high-bandwidth nanopositioning in SPM.

2.1 SPM Operation: AFM Example. The difference between various types of SPMs arises from the type of interaction,

¹Corresponding author.

Contributed by the Dynamic Systems, Measurement, and Control Division of ASME for publication in the JOURNAL OF DYNAMIC SYSTEMS, MEASUREMENT, AND CONTROL. Manuscript received February 6, 2008; final manuscript received April 28, 2009; published online October 28, 2009. Assoc. Editor: J. Karl Hedrick.

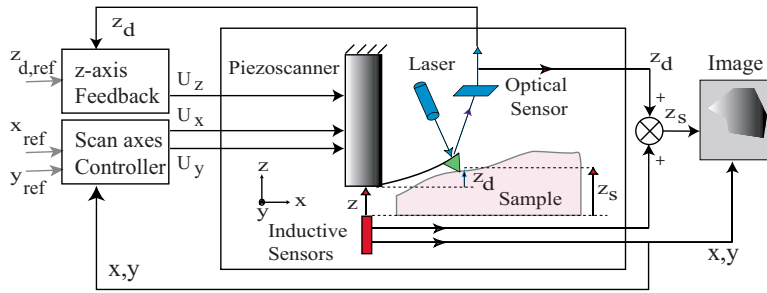


Fig. 1 AFM imaging in contact mode. The AFM probe is positioned using a piezoscanner in the lateral scan (x, y) and vertical (z) axes. Other possible positioning schemes include the sample being moved rather than the AFM probe and the use of separate scanners or multiple stages for different axes.

between the probe and the sample surface, that is measured (or controlled). These include chemical, mechanical, electrical, and magnetic interactions. Moreover, SPM operation is differentiated by whether the probe-sample interaction is kept constant (e.g., in contact mode) or varied (e.g., in tapping mode or during nanofabrication) [3]. To illustrate typical SPM operation, consider contact-mode imaging using an AFM (illustrated in Fig. 1), where the force between the AFM probe and the sample (i.e., the probe-sample interaction) is maintained close to a desired value while the sample is scanned relative to the probe.

Common to all SPMs is the need to scan/position a probe over the sample surface. For example, in contact-mode AFM imaging, the AFM probe (the tip of an AFM cantilever) is scanned in a raster pattern across the sample surface by using a piezoscanner as illustrated in Fig. 1. While scanning the sample surface, the applied probe-sample force is estimated by measuring the deflection z_d of the AFM probe [13]. It is noted that the probe-sample force depends on the relative vertical position of the AFM probe with respect to the sample surface. Therefore, to maintain a constant probe-sample force, the measured AFM-probe deflection is fed back to generate an input U_z that adjusts the vertical position z of the piezoscanner. This adjustment aims to maintain the AFM-probe deflection z_d at the desired value $z_{d,ref}$. Then, an AFM image of the sample topography is obtained, in this case, by plotting the vertical position z_s (of the AFM-probe's tip over the sample) against the lateral x - y position, as illustrated in Fig. 1.

2.2 The Need for High-Speed SPM. SPMs can be used to (a) image and (b) manipulate dynamic surface phenomena at the nanoscale. For imaging and manipulating rapid dynamic processes, high-speed SPMs are needed, as described below.

2.2.1 High-Speed Imaging. Distortion in the SPM-image occurs if the surface property being investigated changes rapidly in time in comparison to the SPM's operating speed. The image distortion arises because measurements at the initial pixel and at the final pixel of an image are acquired at significantly different time instants when the SPM-probe scans over the sample. Therefore, a high-speed SPM is needed to minimize the distortion for studying, manipulating, and controlling processes with fast dynamics. For example, increases in the SPM's operating speed will advance the discovery and understanding of dynamic phenomena by enabling (a) the study of rapid melting and crystallization of polymers [14–16]; (b) the investigation of fast phase transitions in ferroelectric materials [7] that influences domain formation, which in turn affects physical properties (e.g., piezoelectricity, electro-optical properties, and hysteresis); and (c) single-molecule vibrational and force spectroscopies to elucidate structural and electronic information [17,18].

2.2.2 High-Speed Nanofabrication. The main advantage of SPM-based nanofabrication is that it achieves high-resolution

(atomic-scale) features [5]. Unfortunately, SPM-based nanofabrication suffers from throughput limitations that are present in all serial techniques—the SPM-probe must visit each point where operation is needed. Even with multiple probes [19,20], such serial processes cannot compete with parallel techniques such as optical lithography, which can process an entire wafer (more precisely, one die) in one step. A solution to the low-throughput problem is to integrate the slower, top-down, SPM nanofabrication with faster, bottom-up, nanofabrication methods. For instance, rather than adding all the required materials in a direct write approach, STM-based chemical vapor deposition (CVD) might be used only for “seeding” or pre-nucleating the desired pattern, whereas the rest of the material can then be grown by selective CVD [21]. Similarly, patterned self-assembled monolayers can be fabricated with AFM-based dip-pen nanolithography, which can then be used for nucleation and growth of functional polymers [22,23]. In this sense, the top-down SPM is only needed for generating the initial pattern, which then forms the basis for growing the nanostructure using highly parallel bottom-up techniques [24,25]. The SPM-based fabrication of the initial seed pattern is faster than fabrication of the entire features; however, it is still slower than optical lithography methods. Therefore, high-speed SPMs are required to increase the throughput of emerging SPM-based nanofabrication techniques.

2.3 The Need for Nanopositioning in SPMs. Nanopositioning is critical in SPM applications. Broadly, two types of positioning are needed: (a) lateral positioning in the scan x - y axes (see Fig. 1) and (b) vertical positioning along the z axis.

2.3.1 Importance of Precision Lateral (x and y) Positioning. Precision lateral positioning is important when manipulating/modifying the surface at a specific location on the sample, e.g., during nanofabrication. For example, the SPM-probe needs to move along specified scan trajectories x_{ref} and y_{ref} (see Fig. 1) where surface manipulation is required during nanofabrication [5]. Lateral positioning errors lead to distortion of the achieved nanoscale features; therefore, nanopositioning is needed during nanofabrication. In contrast to nanofabrication applications, lateral position is not critical in imaging applications, but desirable. In particular, during imaging applications, precision x and y positioning is desirable to:

- ensure that the desired image area (size) is achieved
- attain a uniform scan speed over the sample (by using a triangular time trajectory for scanning) to control scan-speed-dependent effects in the measurements [26]—scan-speed variations cannot be avoided completely because acceleration is prevalent in turnarounds of the trajectory
- enable uniform spatial resolution across the image when using uniform time-sampling of the data (along with a triangular scan trajectory)

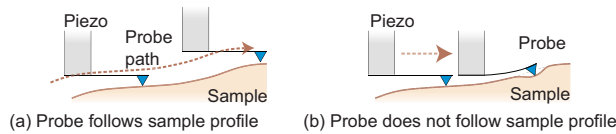


Fig. 2 Precision vertical positioning allows the AFM probe to follow the sample profile (plot (a)) along each scan line without excessive probe deflection and, therefore, without excessive probe-sample force. If the AFM probe does not follow the sample profile (plot (b)), then the probe can “dig” into the sample, causing excessive probe deflection, thereby resulting in excessive probe-sample forces.

- (d) avoid exciting oscillations in the vertical z -axis position of the SPM-probe caused by unwanted oscillations in lateral position due to the coupling between the lateral and vertical dynamics [27].

An advantage of imaging applications over nanofabrication applications is that positioning errors in the scan direction can be alleviated by measuring the achieved x and y positions and then using the measured values, rather than the reference trajectories x_{ref} and y_{ref} , to plot the images; the use of reference trajectories was common practice before sensors were available in SPMs for measuring the lateral x and y positions [10]. Thus, positioning error (e.g., $x \neq x_{ref}$) can be corrected in imaging applications by using position measurements. However, position measurements cannot be used to correct distorted surface features, due to positioning errors, in fabrication processes.

2.3.2 Importance of Precision Vertical (z) Positioning. Vertical positioning is critical for both imaging and manipulation/modification of samples. For example, during contact-mode AFM imaging, the vertical z -axis position, relative to the sample surface, affects the probe-sample force. Ideally, if the AFM-probe's position z_s precisely follows the sample's topography, i.e., the sample profile along each scan line as shown in Fig. 2(a), then the AFM-probe deflection (and the probe-sample force) can be zero. However, it is difficult (if not impossible) to maintain zero, probe-sample forces in practice. In particular, probe-sample forces tend to be nonzero during the initial approach to the sample when the probe-sample force transitions from a repulsive to an attractive regime, and the probe “snaps into” the surface. Moreover, a nonzero, probe-sample force is needed during scanning to maintain contact between the AFM probe and the sample in the presence of disturbances such as thermal noise. Nonetheless, it is important to track the sample profile with nano- (or subnano-) scale precision. If the SPM-probe's tracking of the sample profile contains large errors, as illustrated in Fig. 2(b), then the resulting excessive probe-sample force can cause large sample deformation in soft

samples (the original sample topography profile is then substantially different from the AFM-probe position z_s), as well as sample modification, and, possibly, sample damage. Even when imaging relatively hard samples—where sample damage is not a significant concern—vertical positioning to track the sample profile is still important because excessive probe-sample forces (due to large positioning errors) could damage the AFM probe.

Vertical nanositioning is also critical when modifying the surface. For example, nanoscale features can be fabricated by using the AFM probe as an electrode to induce local-oxidation through an electrical field applied between the AFM probe and the surface [28]. The vertical position of the AFM probe with respect to the sample has a dominant effect on the applied current and the formation of the current-induced oxide, i.e., on the features (size and shape) of the nanofabricated parts [29]. Therefore, precision vertical positioning is important to control the probe-sample interaction being used to create the nanofeatures and, thereby, to avoid feature defects.

3 Limits to SPM Operating Speed

The scanning motion tends to introduce vibration-caused error in the SPM-probe positioning, which, in turn, limits the operating speed of SPMs.

3.1 Why Is Position Control in SPM Difficult? Precision SPM-probe positioning is challenging because piezoscanners not only share typical positioning issues with other piezoactuator-based nanositioners, but also have large model uncertainties related to variations in the operating conditions.

Typical nanositioning problems with piezoactuators. SPM-probe positioning with a piezoscanner needs to account for (a) creep, (b) vibration, and (c) hysteresis [30]. For a recent review, on typical nanositioning issues, see Ref. [11]. The vibration dynamics (see Fig. 3(a) from Ref. [31]) tend to have a low gain margin because of the rapid phase-drop associated with the small structural damping (i.e., sharp resonant peak) that is compounded by the effects of higher-frequency dynamics. Moreover, nonlinearities such as hysteresis effects (see Fig. 3(b)) add to the challenge of designing nanositioning controllers.

Problems specific to SPM. SPM-probe positioning should account for substantial uncertainty in the positioning dynamics due to varying contact conditions between the probe and the sample [32,33], as well as the difficulty in modeling phenomena such as meniscus interactions and viscous damping when operating SPM (probes) in liquid environments [34]. Moreover, SPM-probe positioning needs to account for significant coupling between positioning along different axes. For example, lateral positioning can significantly affect the positioning [27,35], as well as sensing [36,37], in the vertical direction. This is because oscillations in lateral position appear as extraneous variations in the sample topography that need to be tracked in the vertical direction; there-

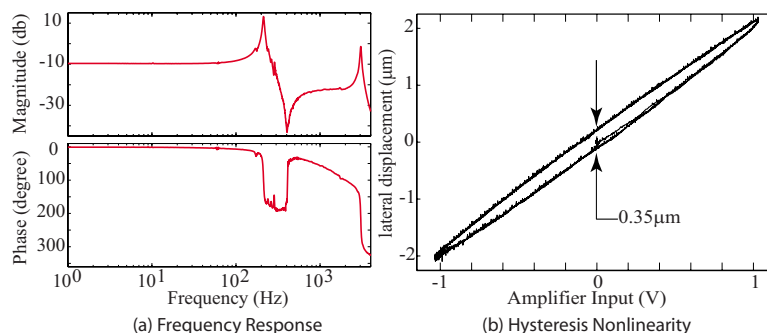


Fig. 3 Experimental (a) frequency response with sharp resonances and (b) hysteresis nonlinearity for a tube-type piezoscanner. The input is the applied voltage to a piezoscanner preamplifier and the output is the lateral displacement. Additional details are provided in Ref. [31].

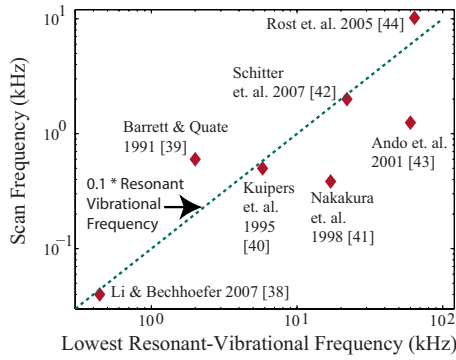


Fig. 4 Scan frequency is around 1/100 to 1/10 of the lowest resonant-vibrational frequency for a variety of SPM positioning systems and different positioning controllers [38–44]

fore, lateral and vertical positioning are coupled even when separate positioners are used for the lateral and vertical positioning.

Overall, low gain margins, nonlinearities, coupling effects, and model uncertainties make precision positioning of the SPM-probe challenging during high-speed SPM operation.

3.2 Resonant-Vibrational Frequency Limits Scan Frequency. Positioning error caused by motion-induced vibration in the SPM-probe positioner (e.g., AFM piezoscanner in Fig. 2) is a significant limitation to high-speed operation of SPMs. As the scan frequency is increased, relative to the lowest resonant-vibrational frequency of the SPM-probe positioner, the vibrational modes of the positioner are excited, resulting in a loss of positioning precision. The vibration-caused positioning error tends to increase with the scan frequency because the major frequency components in the scan trajectory increase toward the resonant-vibrational frequencies of the positioning system. For example, a triangular scan trajectory tends to excite the positioner vibration at a lower scan frequency, when compared with a sinusoidal scan trajectory, because the triangular scan trajectory contains high-frequency harmonics of the scan frequency, which are not present in a sinusoidal scan trajectory. The increase in the vibration-caused positioning error with the scan frequency limits the maximum acceptable scan frequency and, thereby, limits the maximum SPM operating speed. Typically, depending on the resolution needed, the achieved scan frequency is 1/100 to 1/10 of the lowest resonant-vibrational frequency. For example, the plot of SPM scanning frequency versus first resonant-vibrational frequency is shown in Fig. 4 for a variety of SPM positioning systems and different positioning controllers [38–44]. As seen in the figure, the lateral scanning frequency is approximately 10% of the lowest resonant-vibrational frequency.

Other vibration effects. The positioning error caused by exciting the positioner vibration is different from those caused by vibration transmitted to the SPM from external sources. External vibration problems can be addressed using vibration-isolation schemes [45]. Another potential source of errors is vibration in the SPM-probe; e.g., when low stiffness (soft) cantilevers are used to image/manipulate soft samples with an AFM. However, recent probe designs reduce mass and stiffness simultaneously [46] and, thereby, achieve high resonant-vibrational frequencies in soft SPM-probes. The resonant-vibrational frequencies of these new probes are greater than 100 kHz [47], which tend to be substantially higher than the SPM-probe positioner’s resonant-vibrational frequencies in typical SPMs. Therefore, other vibration effects (such as external vibrations and probe softness) are not the major limitations to increasing the SPM’s operating speed at present.

3.3 Increasing the Resonant-Vibrational Frequency. Since the piezoscanner’s lowest, resonant-vibrational frequency limits the achievable scan frequency, an approach to enable nanoposi-

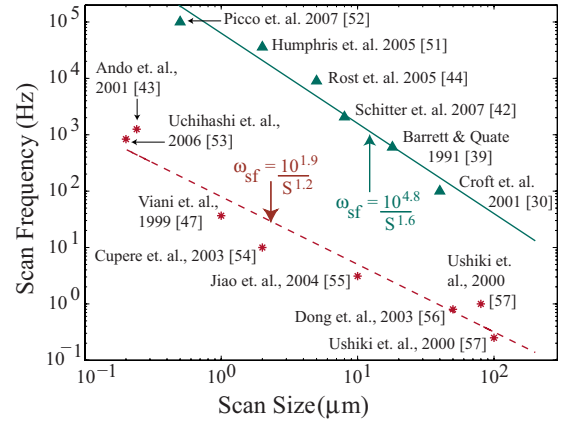


Fig. 5 SPM scan frequency ω_{sf} versus scan size S with a variety of positioning systems operating in air (represented by solid triangles), and in liquid over soft samples (represented by *). The lines are linear least-square-error fits of the data points, solid line for air imaging, and dashed line for liquid imaging. When not reported, the scan frequency and scan size were estimated (if possible) from the images, frame rates, and number of pixels [51–57].

tioning at high scan frequencies is to increase the resonant-vibrational frequencies of the piezoscanner. Using stiffer piezoplates [48] or miniaturized SPMs can increase the scan frequency because the resonant-vibrational frequencies of smaller (and therefore stiffer) piezoscanners tend to be higher [20,40–49]. For example, the first bending resonant-vibrational frequency ω_1 , for an unloaded tube-type piezoscanner, is given by

$$\omega_1 = \frac{1.875^2}{L^2} \sqrt{\frac{EI}{\rho A}} = \frac{1.875^2}{4L^2} \sqrt{\frac{E[D^2 + (D-2h)^2]}{\rho}} \quad (1)$$

where ρ is the mass density, $A = [D^2 - (D-2h)^2]\pi/4$ is the cross-sectional area, D is the outside diameter of the tube, h is the tube thickness, $I = [D^4 - (D-2h)^4]\pi/(4 \times 16)$ is the cross-sectional area moment of inertia, L is the tube length, and E is Young’s modulus. Note that the resonant-vibrational frequency ω_1 is inversely proportional to the square of the piezoscanner length. Therefore, as the piezoscanner length reduces, the scan frequency and the SPM operating speed increase.

Decrease in scan range with smaller piezo. A consequence of increasing the SPM speed (scan frequency) by using smaller piezoscanners is that the scan range R of the piezoscanner reduces with the piezoscanner length L . For example, the maximum lateral displacement (range R) of a tube-type piezoscanner is given by [50]

$$R = \frac{2\sqrt{2}d_{31}L^2 v_{\max}}{\pi D h} \quad (2)$$

where d_{31} is the piezoelectric strain constant and v_{\max}/h is the maximum, applied electric field, which is limited by material properties. Thus, the scan range decreases as the piezoscanner is shortened.

Tradeoff between scan frequency and scan range. Eliminating the length L from the above two equations yields

$$\omega_1 = 0.8d_{31} \frac{v_{\max}}{h} \frac{1}{R} \sqrt{\frac{E}{\rho} [1 + (1-2h/D)^2]} \propto \frac{1}{R} \quad (3)$$

Therefore, the first resonant-vibrational frequency ω_1 is inversely proportional to the scan range R . Similar to this relationship between the first resonant-vibrational frequency ω_1 and the scan range R in Eq. (3), there is an inverse relationship between the achievable SPM scan frequency ω_{sf} and scan size S in reported SPM systems, as shown in Fig. 5. In general, the achieved scan

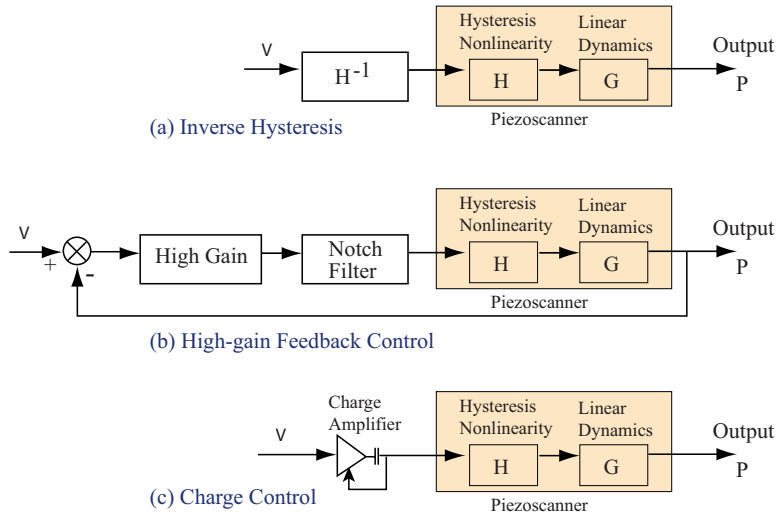


Fig. 6 Three different approaches to linearize hysteresis nonlinearity in piezoscanners

frequency ω_{sf} tends to be lower than the first resonant-vibrational frequency ω_1 , and the achieved scan size S tends to be smaller than the maximum scan range R . A linear least-square-error fit of the data in Fig. 5, which represents a variety of SPM-probe positioning systems, yields

$$\omega_{sf} \propto 1/S^{1.6} \quad \text{for imaging in air}$$

and

$$\omega_{sf} \propto 1/S^{1.2} \quad \text{for imaging in liquid} \quad (4)$$

This inverse relationship dictates the tradeoff between the achieved SPM scan size S and the associated maximum scan frequency ω_{sf} .

Optimizing the tradeoff between scan frequency and scan size. Recent efforts on nanopositioning aim to optimize the tradeoff between scan frequency and scan range. The approach is to augment the displacement of piezoactuators by using flexural-stage designs. Such designs aim to amplify the positioning range while minimizing the reduction in the resonant-vibrational frequencies [42,58–62]. The systems in Refs. [60–62] have not been applied to SPM operations yet, scan frequency of the SPM-images was not reported in Ref. [58], and the system in Ref. [59] was relatively slow since it was not optimized for high-speed operation; therefore, they are not included in Figs. 4 and 5. It is expected that these design approaches will increase the SPM scan frequencies for a given scan size in the future. Nevertheless, vibrational resonance is still present in these nanopositioning systems; reducing the vibration-caused positioning error can increase the SPM operating speed further.

4 Use of Feedforward Approach in High-Speed SPM

The central idea is that feedforward inputs to achieve nanopositioning in high-speed SPM can be found by inverting the piezoscanner dynamics, as first demonstrated in Refs. [12,30]. To illustrate the approach, let G be the map between the input voltage $V(\cdot)$ and the output position $P(\cdot)$ of the piezoscanner

$$P(\cdot) = G[V(\cdot)] \quad (5)$$

Then, to track precisely a given time trajectory of the desired output position $P_d(\cdot)$, the feedforward input $V_{ff}(\cdot)$ can be found by inverting the input-output map G as

$$V_{ff}(\cdot) = G^{-1}[P_d(\cdot)] \quad (6)$$

With choice in position trajectory. When there is flexibility in the choice of position trajectory P_d , e.g., the lateral (x and y)

trajectories used in SPM imaging, other feedforward methods, besides inverse feedforward, can be used. Such feedforward methods include (a) the input-shaping approach to minimize excitation of piezoscanner vibrational modes [63], (b) the optimization of scan trajectories to achieve a constant speed scan in one direction and minimize the retrace time [64], and (c) the reduction of the energy of the input signal at high frequencies to account for actuator limitations [65].

Without choice in position trajectory. When there is no flexibility in the choice of position trajectory P_d , e.g., the lateral (x and y) trajectories used to fabricate specified features with SPM-based nanofabrication, then the inverse input (in Eq. (6)) becomes the ideal feedforward input because it leads to perfect tracking in the absence of external perturbations and modeling errors. The challenges, then, are to address errors in the model used to find the inverse feedforward V_{ff} , and to integrate the feedforward input with feedback to handle external perturbations. These issues are discussed in this section.

4.1 Linearizing the Hysteresis Nonlinearity Before Inversion. The hysteresis nonlinearity is typically linearized (see different schemes in Fig. 6) before using inversion (as in Eq. (6)) to obtain the feedforward input [30]. For example, inversion-based hysteresis compensation, see schematic in Fig. 6(a), can linearize the piezoscanner dynamics for SPM control as demonstrated in Refs. [30,66]. It is noted that inversion of the hysteresis nonlinearity, for general nanopositioners, has been studied extensively in literature; e.g., see recent reviews in Refs. [11,67]. Such inversion-based feedforward can correct for hysteresis effects with high precision; the drawback is the substantial modeling complexity. An alternative approach (without the modeling complexity) is to reduce the hysteresis effects using high gain feedback. In this approach shown in Fig. 6(b), notch filters are used to increase the gain margin of the system as studied in Ref. [68]. Higher gain margin allows the use of higher-gain feedback, which substantially reduces the hysteresis nonlinearity [69]. A third approach is to use charge amplifiers (rather than voltage amplifiers) to drive the piezoscanner, which reduce the hysteresis nonlinearity, as shown in Fig. 6(c) [70–72]. The advantages of the charge control approach, which has been successfully applied to SPM in Ref. [73], are that it eases implementation, does not require position sensing and feedback, and obviates the need for detailed hysteresis modeling and inversion.

An example of a linearized piezoscanner (using a charge amplifier) is shown in Fig. 7. The hysteresis nonlinearity was reduced from 0.35 μm to 0.06 μm ; compare Figs. 3(b) and 7(b) [31]. The

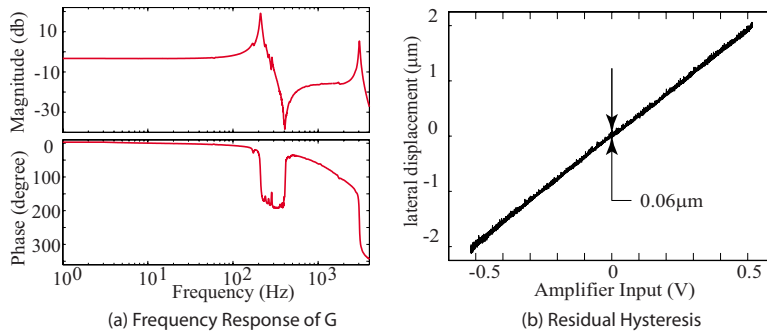


Fig. 7 Experimental (a) frequency response G and (b) residual hysteresis nonlinearity for the tube-type piezoscanner and output range of $4 \mu\text{m}$ as in Fig. 3. The input is the voltage applied to the charge amplifier as in Fig. 6(c) and the output is the lateral displacement. Additional details are in Ref. [31].

resulting linearized piezoscanner, with dynamics G from input V to output P with any of the hysteresis linearization approaches in Fig. 6, can be used with the integrated feedback/feedforward schemes discussed below.

4.2 Integration of Feedforward and Feedback Controllers.

Although this article does not focus on feedback controller design, it is noted that feedback control has been an essential part of SPM development. For example, integral controllers are very effective in maintaining the desired level of probe-sample interaction, particularly during low-speed operation, as they can overcome both creep and hysteresis effects (in the piezoscanners) and the vibrational dynamics are not dominant at low frequencies. In this sense, traditional proportional-integral-derivative (PID) feedback controllers or a double integral for tracking a ramp are well suited for nanopositioning and, therefore, have become popular in low-speed SPM applications [10]. Recent works have aimed to robustify such traditional integral controllers in SPMs [74]. Starting with the early work in Ref. [75], modern feedback control techniques [58,76–79] have been successfully applied to SPM. See Ref. [80] for a comparative review of different feedback methods in SPM. Two approaches used to integrate feedforward and feedback in SPM are illustrated in Fig. 8. These approaches, compared in Ref. [81], are briefly discussed below.

Closed-loop inversion. In general, the model-inversion-based feedforward approach cannot correct for positioning errors due to model uncertainties [85]. Nevertheless, feedback can be used to reduce the effects of piezoscanner uncertainty in the closed-loop system G_{cl} . Then, as shown in Fig. 8(a), the closed-loop system G_{cl} is inverted to obtain the feedforward input

$$V_{ff}(\cdot) = G_{cl}^{-1}[P_d(\cdot)] \quad (7)$$

This closed-loop inversion approach (that reduces the model uncertainty before inversion) reduces the computational error in the feedforward input as demonstrated in Refs. [38,82,83]. Moreover, both the feedback and the inverse feedforward can be simultaneously optimized [81] to improve the positioning performance as demonstrated for SPM control in Refs. [86,87].

Plant inversion. In the plant-inversion approach, shown in Fig. 8(b), the exact positioning feedforward input $V_{ff}(\cdot)$ is the inverse of the piezoscanner dynamics G , as shown in Eq. (6). With this inverse input, $V_{ff}(\cdot) = G^{-1}[P_d(\cdot)]$, the tracking error is zero in the absence of modeling errors and external perturbations—such errors are corrected using feedback. An advantage of the plant-inversion approach is that it tends to have better positioning performance than the closed-loop-inversion approach. This is because the inverse feedforward, with the plant-inversion approach, does not share the performance limitations of the closed-loop system, which arise because feedback controllers trade off positioning performance (such as bandwidth) to ensure stability under plant uncertainties. Additionally, the nonminimum-phase nature of typical piezoscanner dynamics, as well as input saturation bounds, tends to limit the performance of the closed-loop system [58]. The disadvantage of the plant-inversion approach is that it cannot be used in the presence of large model uncertainty, especially, when iterative procedures [27] are not applicable to reduce the uncertainty-caused error, e.g., lateral positioning in nonrepetitive nanofabrication. In such applications, the model uncertainty needs to be reduced by identifying the model under the specific operating conditions.

4.3 Inversion Approaches. This subsection reviews the use of the inversion-based approach to find feedforward inputs that correct for the piezoscanner dynamics and, thereby, enable nanopositioning of the SPM-probe. In the following, the plant-inversion approach (Eq. (6)) is described. The procedure is similar for the closed-loop inversion approach (Eq. (7)) in which the closed-loop transfer function G_{cl} is used instead of the plant transfer function G .

4.3.1 Piezoscanner Model. To illustrate different issues in inversion, consider the following model $G(s)$ of the linearized piezoscanner for positioning along a single axis (lateral or vertical)

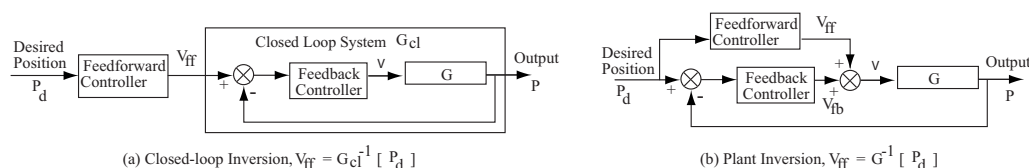


Fig. 8 Integrating feedforward with feedback in SPM: (a) Closed-loop-inversion approach [38,82,83] and (b) plant-inversion approach [27,84]

Table 1 Natural frequencies and damping ratios of linearized model (G in Eq. (8))

	ω (rad/s)	ζ
Zeros	$\omega_z = 2\pi 1000$	$\zeta_z = 0.1$
First resonance poles	$\omega_{p1} = 2\pi 500$	$\zeta_{p1} = 0.05$
Second resonance poles	$\omega_{p2} = 2\pi 3000$	$\zeta_{p2} = 0.05$

$$G(s) = \frac{P(s)}{V(s)} = K \frac{[s^2 - 2\zeta_z \omega_z s + \omega_z^2]}{[s^2 + 2\zeta_{p1} \omega_{p1} s + \omega_{p1}^2][s^2 + 2\zeta_{p2} \omega_{p2} s + \omega_{p2}^2]} \quad (8)$$

where the output P is in nanometers and the input V is in volts. In the following, K is chosen to be 10^{10} and the other parameters are given in Table 1. With this choice of parameters, the dc-gain

$$G(0) = \frac{K \omega_z^2}{\omega_{p1}^2 \omega_{p2}^2} \quad (9)$$

becomes $G(0) = 112.6$ nm/V, which is a typical displacement-per-volt range for tube-type piezoscanners. For example, with a tube-type piezoscanner with $L = 10$ cm, $h = 1$ mm, $D = 1$ cm, and $d_{31} = 0.17$ nm/V (for PZT-5A material [88]), Eq. (2) yields a lateral displacement-per-volt of 153 nm/V. The second vibrational frequency ω_{p2} is chosen to be approximately six times the first vibrational frequency ω_{p1} , and the zero ω_z is interlaced between the poles to represent bending vibrations in beams. The frequency response of the example system (with the above parameter values) is shown in Fig. 9(a).

The piezoscanner dynamics (a) is stable; (b) has zeros on the right half of the complex plane, i.e., is nonminimum phase, as in typical SPM positioning systems, e.g., Refs. [12,58]; and (c) has relative degree of 2. The relative degree, the difference between the order of the transfer function's denominator and numerator, being 2 implies that the input voltage V can directly change the second derivative of the output [89]. Thus, in this case, the input directly changes the acceleration of the output position P as in typical mechanical systems. Note that the use of filters to smooth the input or the output tends to increase the relative degree of the system.

4.3.2 dc-Gain Inverse. The simplest feedforward method is dc-gain inversion, where the feedforward input $V_{ff}(t)$ is found as

$$V_{ff}(t) = [G(0)]^{-1} P_d(t) \quad (10)$$

where P_d is the desired output (position) trajectory. This method works adequately for slow desired trajectories, but results in significant vibration (and positioning error) as the operating frequency is increased because the dynamics are not accounted for.

Positioning error analysis. The positioning error $e = P_d - P$ with the dc-gain approach increases with the frequency content, as well as the amplitude A_p of the desired trajectory. The error dynamics can be obtained (from Eqs. (8) and (10)) as

$$e(s) = P_d(s) - G(s)V_{ff}(s) = \left[1 - \frac{G(s)}{G(0)} \right] P_d(s) = G_e(s)P_d(s) \quad (11)$$

The steady-state error when the desired position is a sinusoidal of frequency ω , say,

$$P_d(t) = A_p \sin(\omega t) \quad (12)$$

is given by

$$e(t) = A_p |G_e(j\omega)| \sin[\omega t + \angle G_e(j\omega)] \quad (13)$$

Then, the maximum positioning error e_{\max} and the percent maximum positioning error $\%e_{\max}$, at the steady state, are given by

$$e_{\max} = A_p |G_e(j\omega)| \quad (14)$$

$$\%e_{\max} = 100 e_{\max} / A_p = 100 |G_e(j\omega)|$$

where $|G(j\omega)|$ and $\%e_{\max}$ are shown for different frequencies ω in Fig. 9.

Note that the maximum positioning error e_{\max} increases with both (a) the amplitude of the position trajectory A_p , as well as (b) the frequency ω that needs to be tracked. Therefore, for the same amount of acceptable positioning error e_{\max} , the maximum positioning frequency ω_{\max} reduces as the amplitude of the position trajectory A_p increases. For example, with an acceptable maximum error $e_{\max} = 20$ nm and amplitude $A_p = 1$ μm , the maximum percentage error needs to be less than 2%, which occurs at 43.3 Hz in Fig. 9(b)—this is slightly less than one-tenth of the first resonant-vibrational frequency at 500 Hz. If the positioning amplitude is increased ten times to $A_p = 10$ μm , then the maximum percentage error needs to be less than 0.2% and the maximum scan frequency is reduced to 4.54 Hz. Nevertheless, the dc-gain approach can be used when the position trajectories' frequency components are sufficiently low in comparison to the resonant-vibrational frequencies of the piezoscanner.

4.3.3 Inverting Periodic Trajectories. When the position trajectory is periodic, e.g., for lateral scanning, the computation of the inverse (in Eq. (18)) can be simplified using steady-state solutions as in Refs. [83,90,91]. In particular, let the desired position P be periodic; i.e.,

$$P_d(t) = \sum_k A_k \sin[\omega_k t + \psi_k] \quad (15)$$

Then, the inverse feedforward (in Eq. (6)) can be computed as [83]

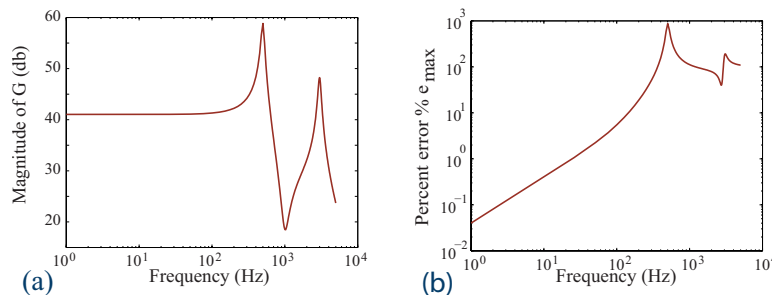


Fig. 9 (a) Magnitude response of example system G in Eq. (8) and (b) percentage error $\%e_{\max}$ in Eq. (14) for a sinusoidal position trajectory. The percentage error reaches 2% at 43.3 Hz, which is slightly less than one-tenth of the first resonant-vibrational frequency at 500 Hz.

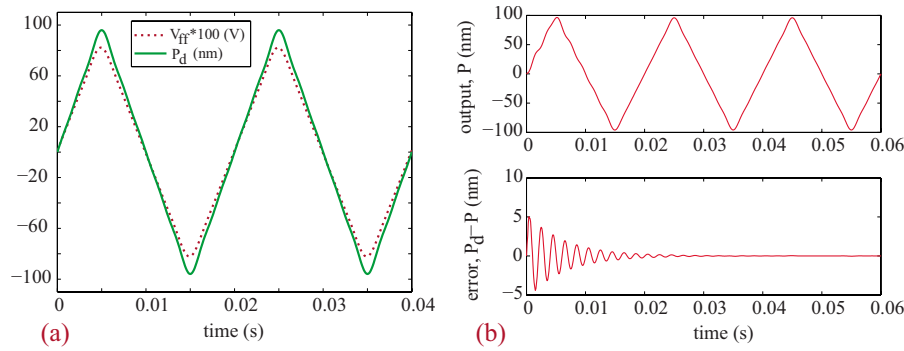


Fig. 10 Inversion for periodic position trajectory. (a) Feedforward input V_{ff} and desired position P_d for system G in Eq. (8). (b) Simulated transient error ($P_d - P$) in position P when the periodic inverse input V_{ff} is applied to G .

$$V_{ff}(t) = \sum_k \frac{A_k}{|G(j\omega_k)|} \sin[\omega_k t + \psi_k - \angle G_x(j\omega_k)] \quad (16)$$

For example, the feedforward input V_{ff} when the desired position P_d is the first five odd harmonics of a 50 Hz triangular trajectory

$$\omega_k = k(2\pi 50), \quad A_k = 100 \frac{8}{\pi^2} \frac{(-1)^{(k-1)/2}}{k^2}, \quad \psi_k = 0 \quad \text{for } k = 1, 3, 5, 7, 9 \quad (17)$$

is shown in Fig. 10(a) for the system G in Eq. (8). While the approach does not address transient vibration, the error in the resulting position (due to initial condition mismatch) decreases exponentially as shown in Fig. 10(b), because the piezoscanner dynamics G is stable. For this simulation, the positioning error reduces to less than 5×10^{-3} nm after 3 cycles. In general, the time needed for the transient error to become sufficiently small depends on the poles of the system $G(s)$.

Application of periodic-trajectory tracking in SPM. An advantage of this periodic-trajectory inversion is that for tracking a purely sinusoidal trajectory of frequency ω , it requires the estimation of two parameters, $|G(j\omega)|$ and $\angle G(j\omega)$, which could be identified online. This approach is well suited to lateral control in SPM for imaging applications, if images are acquired after the transient error becomes small as demonstrated in Ref. [90]. The approach can also be adapted to identify the SPM dynamics as shown in Ref. [91].

Extension to repetitive control (RC). The formulation as the tracking of a periodic trajectory lends itself to techniques from repetitive control [92,93] that can be applied to nonminimum-phase systems [94]. In such applications, the periodic input in Eq. (16) can be found by exploiting the internal model principle [95], where asymptotic tracking of the desired output is achieved provided the generator for the desired output is included in the stable, closed-loop system. An advantage of the repetitive control approach is that it can be easily integrated into an existing feedback controller in SPMs to handle tracking error associated with periodic motion and/or to reject periodic exogenous disturbances [96]. Recently, the applicability of repetitive control methods to lateral positioning in SPM was demonstrated in Refs. [96,97].

4.3.4 Exact Inverse as Feedforward. If the linearized dynamics is minimum phase (no zeros on the open right half of the complex plane), then the inverse feedforward can be found by inverting the system dynamics [98]

$$V_{ff}(s) = G^{-1}(s)P_d(s) \quad (18)$$

Inverse is not proper. An issue with the exact inverse in Eq. (18) is that the inverse $G^{-1}(s)$ is not proper. The input voltage V directly changes the r th time derivative of position P , where r is the relative degree (the difference between the orders of the de-

nominator and numerator polynomials) of the transfer function G [89]. Therefore, the desired position P has to be sufficiently smooth (differentiable r times with respect to time) for exact tracking. For the example system (Eq. (8)), with relative degree $r=2$, the desired position P_d must be twice differentiable (in time) to be tracked exactly. Let $\ddot{P}_d(t) = (d^2/dt^2)P_d(t)$; then, the inverse in Eq. (18) can be rewritten as

$$V_{ff}(s) = \left[\frac{G^{-1}(s)}{s^2} \right] s^2 P_d(s) = [s^2 G(s)]^{-1} \ddot{P}_d(s) = [G^\#(s)]^{-1} \ddot{P}_d(s) \quad (19)$$

where the inverse $[G^\#(s)]^{-1}$ is proper since $G^\#(s) = s^2 G(s)$ is proper with relative degree zero. It is noted that being twice differentiable is a necessary condition for exact tracking and a trajectory $P(t)$ that is not twice differentiable in time cannot be tracked with finite inputs [89]. Therefore, if the trajectory P_d can be tracked, then the need to specify the second time derivative \ddot{P}_d of the position P_d does not impose an additional requirement.

Inverse for nonminimum-phase systems. The exact inverse $G^{-1}(s)$ would be unstable if the system $G(s)$ is nonminimum phase since the right-half-plane zeros of $G(s)$ become the unstable poles of $G^{-1}(s)$. Therefore, a standard inverse (Eq. (18) or Eq. (19)) would result in an unbounded feedforward input $V_{ff}(\cdot)$ over time for a general position trajectory $P(\cdot)$. In contrast, a bounded (although noncausal) feedforward input can be found, for the nonminimum-phase case, using the Fourier-transform approach by Bayo in Ref. [99]. For the example system (Eq. (8)), the exact inverse can be found as

$$V_{ff}(j\omega) = [G^\#(j\omega)]^{-1} \ddot{P}_d(j\omega) \quad (20)$$

Then, the time-domain inverse input V_{inv} is obtained using the inverse Fourier transform. A time-domain interpretation was developed in Ref. [100] and inverse for nonlinear nonminimum-phase systems was developed in Ref. [101].

For the example system (Eq. (8)), the desired acceleration \ddot{P}_d , the desired position P_d , and the exact-inverse feedforward V_{ff} are shown in Fig. 11. The triangular sections of the desired acceleration \ddot{P}_d in Fig. 11 can be described using Eq. (17) with $\omega_k = k(2\pi 500)$ and scaled to generate an output P_d with a maximum displacement of 100 nm. Note that the inverse input V_{ff} found in the Fourier domain remains bounded even though the inverse system $G^{-1}(s)$ has unstable poles. Also, note that the inverse V_{ff} is noncausal—it is nonzero before the output acceleration \ddot{P}_d starts to change as seen in Fig. 11. Therefore, the feedforward input V_{ff} has to be applied a priori, before the output starts to change.

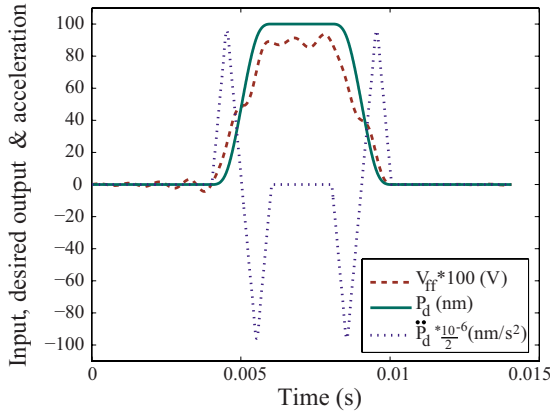


Fig. 11 Noncausal, exact-inverse feedforward V_{ff} for a desired output acceleration \ddot{P}_d and the associated desired output trajectory P_d . Note that the inverse feedforward V_{ff} is nonzero before the output acceleration \ddot{P}_d starts to change.

Exact inversion in the time domain. The time-domain approach to exact inversion is presented below. Let the system G be given in state space form as

$$\dot{x}(t) = Ax(t) + BV(t)$$

$$P(t) = Cx(t) \quad (21)$$

In the following, expressions are provided for the general case of relative degree r ; for the example, expressions can be obtained by setting the relative degree as $r=2$. The relative degree r implies that the input V appears in the expression for the r th time derivative of the output position P as [102]

$$\frac{d^r}{dt^r} P(t) = CA^r x(t) + CA^{r-1} B V_{ff}(t) = A_y x(t) + B_y V_{ff}(t) \quad (22)$$

where B_y is guaranteed to be invertible. The inverse system can be written as [98,102]

$$\begin{aligned} \dot{\eta}(t) &= [A_{inv}] \eta(t) + [B_{inv}] \mathcal{Y}_d(t) \\ V_{ff}(t) &= [C_{inv}] \eta(t) + [D_{inv}] \mathcal{Y}_d(t) \end{aligned} \quad (23)$$

where

$$\begin{aligned} A_{inv} &:= T_\eta [A - (BB_y^{-1}A_y)] T_r^{-1} \\ B_{inv} &:= [T_\eta [A - (BB_y^{-1}A_y)] T_l^{-1} \vdots (T_\eta BB_y^{-1})] \\ C_{inv} &:= -B_y^{-1} A_y T_r^{-1} \\ D_{inv} &:= [(-B_y^{-1} A_y T_l^{-1}) \vdots (B_y^{-1})] \\ \mathcal{Y}_d(t) &:= \begin{bmatrix} \zeta_d(t) \\ \frac{d^r}{dt^r} P_d(t) \end{bmatrix} \end{aligned} \quad (24)$$

and T represents a state transformation

$$\begin{bmatrix} \zeta_d(t) \\ \dots \\ \eta(t) \end{bmatrix} = \begin{bmatrix} P_d(t) \\ P_d^{(1)}(t) \\ \vdots \\ \frac{d^{(r-1)}}{dt^{(r-1)}} P_d(t) \\ \dots \\ \eta(t) \end{bmatrix} = \begin{bmatrix} C \\ CA \\ \vdots \\ CA^{r-1} \\ \dots \\ T_\eta(t) \end{bmatrix} x(t) = \begin{bmatrix} T_\zeta \\ \dots \\ T_\eta \end{bmatrix} x(t) = Tx(t) \quad (25)$$

$$x(t) = T^{-1} \begin{bmatrix} \zeta_d(t) \\ \eta(t) \end{bmatrix} = [T_l^{-1} | T_r^{-1}] \begin{bmatrix} \zeta_d(t) \\ \eta(t) \end{bmatrix} \quad (26)$$

and the bottom portion T_η of the coordinate transformation matrix T in Eq. (25) is chosen such that T is invertible. For the example system G in Eq. (8),

$$\begin{aligned} A &= \begin{bmatrix} 0 & 1 & 0 & 0 \\ -\omega_{p1}^2 & -2\zeta_{p1}\omega_{p1} & 0 & 0 \\ 0 & 0 & 0 & 1 \\ 0 & 0 & -\omega_{p2}^2 & -2\zeta_{p2}\omega_{p2} \end{bmatrix}, \\ B &= \begin{bmatrix} 0 \\ 4.9431 \times 10^4 \\ 0 \\ 4.9431 \times 10^4 \end{bmatrix}, \end{aligned} \quad (27)$$

$$C = [1.7295 \times 10^4 \quad -1 \quad 1.8658 \times 10^5 \quad 1] \quad (27)$$

and with T_η (in Eq. (25)) chosen as

$$T_\eta = \begin{bmatrix} 1 & 0 & 0 & 0 \\ 0 & 0 & 1 & 0 \end{bmatrix} \quad (28)$$

the matrices associated with the inverse system (in Eq. (23)) are given by

$$\begin{aligned} A_{inv} &= \begin{bmatrix} 1.5741 \times 10^4 & 1.7209 \times 10^5 \\ -1.5543 \times 10^3 & -1.4484 \times 10^4 \end{bmatrix}, \\ B_{inv} &= \begin{bmatrix} -9.1295 \times 10^{-1} & 4.9431 \times 10^{-6} & 0 \\ 8.7045 \times 10^{-2} & 4.9431 \times 10^{-6} & 0 \end{bmatrix}, \\ C_{inv} &= [-9.8781 \times 10^1 \quad 5.4687 \times 10^3], \end{aligned}$$

$$D_{inv} = [6.5191 \times 10^{-3} \quad 3.4558 \times 10^{-7} \quad 1 \times 10^{-10}] \quad (29)$$

Remark 1. (Unstable internal dynamics). The eigenvalues of A_{inv} (Eq. (23)), i.e., the poles of the inverse system, correspond to the zeros of the original system $G(s)$ (Eq. (8)). Therefore, the inverse system is unstable for nonminimum-phase systems.

For general hyperbolic systems (with no zeros on the imaginary axis), to find a bounded solution to the unstable inverse system (Eq. (23)), the internal state η is decoupled into stable and unstable states using a coordinate transformation T_{split}

$$T_{split} \begin{bmatrix} \eta_s(t) \\ \eta_u(t) \end{bmatrix} = \eta(t) \quad (30)$$

The new state equation is given by

$$\begin{aligned} \frac{d}{dt} \begin{bmatrix} \eta_s(t) \\ \eta_u(t) \end{bmatrix} &= [T_{split}^{-1}] [A_{inv}] [T_{split}] \begin{bmatrix} \eta_s(t) \\ \eta_u(t) \end{bmatrix} + [T_{split}^{-1}] [B_{inv}] \mathcal{Y}_d(t) \\ &= \begin{bmatrix} A_s & 0 \\ 0 & A_u \end{bmatrix} \begin{bmatrix} \eta_s(t) \\ \eta_u(t) \end{bmatrix} + \begin{bmatrix} B_s \\ B_u \end{bmatrix} \mathcal{Y}_d(t) \end{aligned} \quad (31)$$

Remark 2. The transformation matrix T_{split} is chosen to decouple the internal state η into stable and unstable subdynamics.

The transformation matrix can be found using the eigenvectors of the matrix $[A_{\text{inv}}]$.

Remark 3. For the example system (Eq. (8)), both the poles of A_{inv} are unstable; therefore, the stable portion η_s of the internal dynamics is null.

In general a bounded solution to the decoupled internal state equations

$$\dot{\eta}_s(t) = A_s \eta_s(t) + B_s \mathcal{Y}_d(t)$$

$$\dot{\eta}_u(t) = A_u \eta_u(t) + B_u \mathcal{Y}_d(t)$$

can be found as

$$\eta_{s,\text{ref}}(t) = \int_{-\infty}^t e^{A_s(t-\tau)} B_s \mathcal{Y}_d(\tau) d\tau \quad (\text{solved forward in time})$$

$$\eta_{u,\text{ref}}(t) = - \int_t^{\infty} e^{-A_u(\tau-t)} B_u \mathcal{Y}_d(\tau) d\tau \quad (\text{solved backward in time}) \quad (32)$$

The reference internal state trajectory is then found (from Eqs. (30) and (32)) as

$$\eta_{\text{ref}}(t) = [T_{\text{split}}] \begin{bmatrix} \eta_{s,\text{ref}}(t) \\ \eta_{u,\text{ref}}(t) \end{bmatrix} \quad (33)$$

and the inverse input can be found from Eq. (23) as

$$V_{\text{ff}}(t) = [C_{\text{inv}}] \eta_{\text{ref}}(t) + [D_{\text{inv}}] \mathcal{Y}_d(t) \quad (34)$$

Remark 4. (The need for preview). Computing the bounded solution to the unstable internal state $\eta_{u,\text{ref}}$ at time t required information about future values of the desired output, e.g., $\mathcal{Y}_d(\tau)$ with $\tau > t$ in Eq. (32).

The noncausality of the inverse input V_{ff} implies that the future, desired output trajectory needs to be known (ahead of time) for computing the inverse, e.g., in the Fourier domain (Eq. (20)) or in the time domain (see Remark 4). This is acceptable for lateral positioning in SPM when the desired x and y trajectories are known ahead.

Preview-based implementation of noncausal inverse. In some applications the entire desired position trajectory might not be available, but at any time instant t , future position information might be available for a finite preview-time interval $[t, t+T_p]$. For instance, the lateral position trajectory needs to be changed in nonraster scanning used to image only parts of the scan area that is of interest [103]. In such cases, the inverse feedforward can be computed using the finite preview information of the desired position trajectory. In particular, the bounded solution to the unstable internal state $\eta_{u,\text{ref}}$ at time t only uses finite preview information if its bounded solution in Eq. (32) is approximated as [102]

$$\eta_{u,\text{ref}}(t) = - \int_t^{t+T_p} e^{-A_u(\tau-t)} B_u \mathcal{Y}_d(\tau) d\tau \quad (35)$$

The amount of preview time T_p needed can be quantified in terms of the required tracking accuracy and the system dynamics [102]. Such a preview-based approach was demonstrated for SPM control in Ref. [104]. If sufficient preview time is not available, then, the feedforward can be optimized for minimizing the tracking error for the available amount of preview [105,106].

Causal approximate inverse for nonminimum-phase systems. In some applications, preview information of the output position may not be available, e.g., when tracking the vertical probe-sample distance to correct for surface variations during SPM nanofabrication. For nonminimum-phase systems, the lack of preview in these applications is a major limitation to achieving precision positioning because the noncausal exact-inverse cannot be used. Causal controllers cannot perfectly track general trajectories

when the system is nonminimum phase [107]. The only recourse then is to use causal feedforward approaches that can achieve asymptotic tracking for certain classes of trajectories [89,108], and approximate tracking for more general trajectories, e.g., Refs. [109,110]. A review of approximate inversion is presented in Ref. [81]. If the positioning error (with the causal feedforward) is too large, then the SPM operating speed needs to be reduced so that the position error can be lowered to an acceptable level—thus, limiting the operating speed.

4.4 Inverse Feedforward Under Model Uncertainty. It can be shown that the addition of inverse feedforward can improve the positioning performance when compared with the use of feedback alone, even in the presence of plant uncertainties—the size of acceptable uncertainty is quantified for general linear time-invariant systems in Refs. [87,111]. In particular, for single-input single-output systems, such as SPM-probe positioning along a single axis, performance improvement with the addition of feedforward can be guaranteed at frequencies ω where the uncertainty $\Delta(j\omega)$ in the nominal plant is smaller than the size of the nominal plant $G(j\omega)$ [111] as follows:

$$\Delta(j\omega) < |G(j\omega)| \quad (36)$$

Remark 5. (Noncausality of inverse under uncertainty). Typical systems tend to have large model uncertainties at higher frequencies; the resulting inverse (in frequency regions satisfying Eq. (36)) is noncausal—even if the system G is minimum phase [111]. In particular, if the inverse is set to zero in any frequency interval of nonzero length, then the resulting time-domain input V is noncausal by the Paley–Wiener condition [111].

4.4.1 Optimal Inverse. The acceptable uncertainty bounds, for guaranteed performance improvement with the use of the inverse feedforward (in Eq. (36)), are often violated in typical systems. Most piezoscanners tend to have some frequency regions where plant uncertainty is unacceptably large—usually at high frequencies and near system zeros. Therefore, the inverse should be computed only in frequency regions where the plant uncertainty is “sufficiently” small. The optimal inverse developed in Ref. [112] allows the inverse to be computed at specified frequency ranges. The optimal inverse input is found by minimizing the following cost function that is similar to the cost function used in standard linear quadratic regulators with frequency-dependent weights as in Ref. [113]:

$$J(V) = \int_{-\infty}^{\infty} \{V^*(j\omega)R(j\omega)V(j\omega) + E_p^*(j\omega)Q(j\omega)E_p(j\omega)\} d\omega \quad (37)$$

where $*$ denotes the complex conjugate transpose and $E_p = P_d - P$ is the positioning error. The terms $R(j\omega)$ and $Q(j\omega)$ are real-valued, frequency-dependent weightings that penalize the size of the input V and the positioning error E_p [113].

Remark 6. (Weights for large uncertainty). If the model uncertainty is large at some frequency ω , then the choice of weights $R(j\omega) > 0$ and $Q(j\omega) = 0$ results in a minimum cost with zero input $V(j\omega) = 0$, i.e., no tracking at that frequency.

Remark 7. (Actuator redundancy and deficiency). The above cost function can be used to optimize the input with redundant actuators in multistage positioning systems, and for optimal tracking in actuator deficient systems [114].

The optimal inverse input V_{opt} that minimizes the cost function (in Eq. (37)) can be found, for the single-input-single-output (SISO) case, as [112]

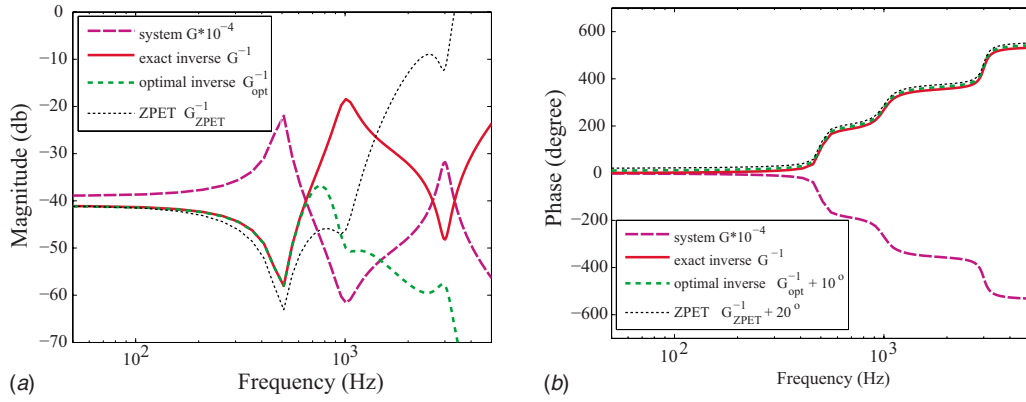


Fig. 12 Comparison of exact inverse G^{-1} , optimal inverse G_{opt}^{-1} , and ZPET inverse G_{ZPET}^{-1} . (a) Magnitude and (b) phase. Note that the phase plots for the optimal inverse and ZPET inverse are shifted to distinguish them from the phase plot of the exact inverse.

$$V_{\text{opt}}(j\omega) = \left[\frac{G^*(j\omega)Q(j\omega)}{R(j\omega) + G^*(j\omega)Q(j\omega)G(j\omega)} \right] P_d(j\omega) = G_{\text{opt}}^{-1}(j\omega)P_d(j\omega) \quad (38)$$

and the time-domain signal for the feedforward input $V_{\text{ff}}(t) = V_{\text{opt}}(t)$ is then obtained through an inverse Fourier transform of $V_{\text{opt}}(j\omega)$. Time-domain computations using impulse response of G_{opt}^{-1} , as well as a preview-based implementation, are discussed in Ref. [104].

Remark 8. (Frequency-weighted inverse). The optimal inverse (in Eq. (38)) can be expressed as

$$G_{\text{opt}}^{-1}(j\omega) = \left[\frac{G^*(j\omega)Q(j\omega)G(j\omega)}{R(j\omega) + G^*(j\omega)Q(j\omega)G(j\omega)} \right] G^{-1}(j\omega) = \rho_{\text{opt}}(j\omega)G^{-1}(j\omega) \quad (39)$$

Therefore, the optimal inverse can be considered as a frequency weighted inverse.

4.4.2 Comparison of Optimal and Exact Inverses. The exact inverse tends to increase at high frequencies where the system G tends to have low gains, especially when the frequency is high in comparison to the first, resonant-vibrational frequency of the positioning system (as shown in Fig. 12). A problem with such an inverse is that modeling uncertainties also tend to be large at higher frequencies. One approach is to suppress exciting the higher-frequency (uncertain) regions by using a relatively large weight on the input (R) at such frequencies in the cost function (Eq. (37)). The weights in the cost functions $Q(j\omega)$ and $R(j\omega)$ are real valued when they have the form

$$R(j\omega) = r^*(j\omega)r(j\omega), \quad Q(j\omega) = q^*(j\omega)q(j\omega) \quad (40)$$

For this example, r and q are chosen to suppress exciting frequencies beyond the main resonant-vibrational frequency (at 500 Hz) as

$$w(s) = \frac{2\pi 500}{s + 2\pi 500}, \quad q(s) = w(s), \quad r(s) = 10/w(s) \quad (41)$$

The resulting optimal inverse G_{opt}^{-1} in Eq. (38) and the exact inverse G^{-1} in Eq. (20) are compared in Fig. 12, for the example system G (Eq. (8)), whose response is also shown in the same plot. The magnitude of the optimal inverse tends to reduce at higher frequencies (by design, to suppress exciting these regions) as shown in Fig. 12. Thus, the optimal inverse enables tradeoffs between the desire to track an output precisely and the need to account for the model uncertainty as well as actuator bandwidth limits [111].

4.4.3 Comparison of Optimal Inverse and ZPET Feedforward.

The optimal inverse achieves the appropriate phase correction at all frequencies as in zero-phase-error-tracking (ZPET) feedforward [109]. In particular, if the weights $Q(j\omega)$ and $R(j\omega)$ are chosen to be zero phase (e.g., as in Eq. (40)), then the optimal inverse in Eq. (38) has the same phase as the exact inverse since ($\angle G^* = \angle G^{-1}$), as shown in Fig. 12(b). Therefore, the optimal inverse has the appropriate phase correction, based on the nominal model, at all frequencies. This is similar to the ZPET feedforward in Ref. [109], where a minimum-phase system G_{ZPET} is used to approximate the nonminimum-phase dynamics by replacing the nonminimum-phase zeros with stable poles before inverting to find the feedforward input. For the example system (Eq. (8)), the ZPET approximation results in

$$G_{\text{ZPET}}(s) = K \frac{\omega_z^4}{[s^2 + 2\zeta_z \omega_z s + \omega_z^2][s^2 + 2\zeta_{p1} \omega_{p1} s + \omega_{p1}^2][s^2 + 2\zeta_{p2} \omega_{p2} s + \omega_{p2}^2]} \quad (42)$$

where the additional pair of poles has the same imaginary parts as the original zeros, but with a change in the sign in the real part. If at some frequency ω , the model uncertainty is not too large for a nonminimum-phase system, then the optimal inverse provides the appropriate magnitude (gain) correction for the nominal plant,

even at high frequencies. In contrast, the ZPET feedforward aims to achieve good magnitude (gain) correction in the low-frequency region and not at high frequencies (as shown in Fig. 12) even if the model uncertainty is zero—due to the replacement of the nonminimum-phase model by a minimum-phase one [109]. Thus,

both the optimal inverse and the ZPET feedforward achieve zero-phase-error tracking; however, the optimal inverse tends to achieve better performance than the ZPET feedforward in high-bandwidth tracking.

4.4.4 Comparison of Optimal Inverse and Robust Feedforward. The optimal inverse G_{opt}^{-1} can be considered as the noncausal generalization of H_{∞} -robust feedforward [115], where the feedforward controller G_{ff} is found by minimizing the worst-case system energy gain [116]

$$J_{H_{\infty}}(G_{\text{ff}}) = \left\| \begin{array}{c} r(\cdot)G_{\text{ff}}(\cdot) \\ q(\cdot)[1 - G_{\text{ff}}(\cdot)G(\cdot)] \end{array} \right\|_{\infty} \quad (43)$$

over all causal, stable controllers G_{ff} to obtain the feedforward input as

$$V_{\text{ff}}(s) = G_{\text{ff}}(s)P_d(s) \quad (44)$$

where $r(s) > 0$ and $q(s) \geq 0$ are frequency-dependent weights as in Eq. (40). It is noted that for any feedforward controller G_{ff} , and any given desired output $P_d(\cdot)$, the integrand I_J in the cost function $J(V)$ for the optimal inverse (in Eq. (37)) can be rewritten as (using Eq. (40), and by substituting $E_p = P_d - P$)

$$\begin{aligned} I_J[V, P_d](j\omega) &= V^*(j\omega)r^*(j\omega)r(j\omega)V(j\omega) \\ &\quad + E_p^*(j\omega)q^*(j\omega)q(j\omega)E_p(j\omega) \\ &= \left\| \begin{array}{c} r(j\omega)V(j\omega) \\ q(j\omega)(P_d(j\omega) - P(j\omega)) \end{array} \right\|_2^2 \end{aligned} \quad (45)$$

for all frequency ω , where $\|a\|_2^2$ is the square of the standard vector 2-norm for $a \in \mathbb{C}^n$. With the feedforward controller G_{ff} , substituting $V = G_{\text{ff}}P_d$ for the input and

$$P = GV = GG_{\text{ff}}P_d \quad (46)$$

for the output, the integrand (in Eq. (45)) can be rewritten in terms of the feedforward controller G_{ff} as

$$I_J[G_{\text{ff}}, P_d](j\omega) = \left\| \begin{array}{c} r(j\omega)G_{\text{ff}}(j\omega)P_d(j\omega) \\ q(j\omega)[1 - G(j\omega)G_{\text{ff}}(j\omega)]P_d(j\omega) \end{array} \right\|_2^2 \quad (47)$$

As shown in Ref. [112], the optimal inverse $V_{\text{opt}} = G_{\text{opt}}^{-1}P_d$ minimizes the cost function $J(V)$ (in Eq. (37)) by minimizing the integrand (in Eq. (45)) at each frequency ω for any desired output P_d . Therefore,

$$I_J[G_{\text{opt}}^{-1}, P_d](j\omega) \leq I_J[G_{\text{ff}}, P_d](j\omega) \quad (48)$$

at each frequency ω . This implies that the integral over the entire frequency domain shares the similar relationship (as the integrand is non-negative at each frequency)

$$\int_{-\infty}^{\infty} \{I_J[G_{\text{opt}}^{-1}, P_d](j\omega)\} d\omega \leq \int_{-\infty}^{\infty} \{I_J[G_{\text{ff}}, P_d](j\omega)\} d\omega \quad (49)$$

which, in turn, results in

$$\sup_{P_d(\cdot) \neq 0} \frac{\int_{-\infty}^{\infty} \{I_J[G_{\text{opt}}^{-1}, P_d](j\omega)\} d\omega}{\|P_d(\cdot)\|_2^2} \leq \sup_{P_d(\cdot) \neq 0} \frac{\int_{-\infty}^{\infty} \{I_J[G_{\text{ff}}, P_d](j\omega)\} d\omega}{\|P_d(\cdot)\|_2^2} \quad (50)$$

where $\|P_d(\cdot)\|_2^2$ represents the square of the functional 2-norm. The above equation implies that the H_{∞} -norms (i.e., the induced function norms) are related as

$$\left\| \begin{array}{c} r(\cdot)G_{\text{opt}}^{-1}(\cdot) \\ q(\cdot)[1 - G(\cdot)G_{\text{opt}}^{-1}(\cdot)] \end{array} \right\|_{\infty} \leq \left\| \begin{array}{c} r(\cdot)G_{\text{ff}}(\cdot) \\ q(\cdot)[1 - G(\cdot)G_{\text{ff}}(\cdot)] \end{array} \right\|_{\infty} \quad (51)$$

Therefore, the optimal inverse minimizes the cost function $J_{H_{\infty}}(G_{\text{ff}})$ (in the H_{∞} -norm) over all feedforward controllers G_{ff} —causal or noncausal, i.e.,

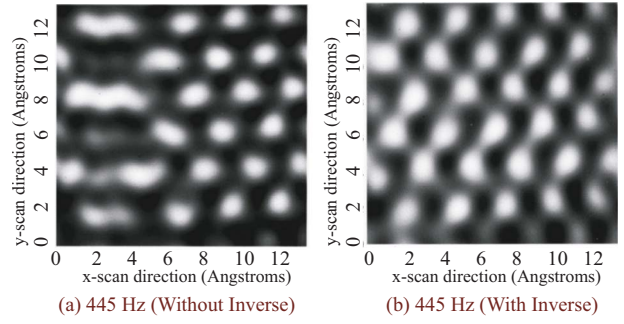


Fig. 13 Comparison of STM images of HOPG surface without (plot (a)) and with (plot (b)) the optimal inverse input [12]. The distortion of the uniform lattice pattern of the sample (in plot (a)) is substantially reduced with the use of the optimal inverse (in plot (b)).

$$J_{H_{\infty}}(G_{\text{opt}}^{-1}) = \inf_{G_{\text{ff}}} [J_{H_{\infty}}(G_{\text{ff}})] \quad (52)$$

Thus, the H_{∞} cost of the optimal inverse is less than or equal (but not more) than the H_{∞} cost for the standard, robust feedforward controller obtained by restricting the solution space to causal controllers.

4.4.5 Application of Optimal Inverse to SPM. The optimal inverse was applied to achieve high-speed imaging with a STM in Ref. [12]. The use of the optimal inverse is comparatively evaluated without the use of the optimal inverse in Fig. 13, which shows STM images of a highly oriented pyrolytic graphite (HOPG) surface. Note that the uniform lattice pattern of the HOPG sample is distorted significantly due to vibration-caused positioning errors in the scan trajectory (Fig. 13(a)). In contrast, the distortion can be reduced by using the optimal-inversion-based feedforward input, and the image captures the expected lattice pattern (Fig. 13(b)). Thus, positioning errors can be reduced with the optimal inverse to increase the SPM's operating speed [12].

4.5 IIC. When the positioning application is repetitive (e.g., during periodic scanning of the SPM-probe), iterative control methods can improve the positioning performance. Therefore, iterative [27,117–122] and adaptive control methods [123] are well suited for SPM applications [11]. For example, uncertainty in the inversion process can be reduced using adaptive inversion of the system model or by learning the “correct” inverse input that yields perfect output tracking, i.e., iterative inversion of the system model [27,124,122]. The application of such iterative control to SPM was demonstrated in Refs. [27,61,91,125,126]. Iterative approaches can also be used to reduce positioning errors due to hysteresis as demonstrated in Refs. [8,127].

4.5.1 IIC Procedure. The inverse G^{-1} was used in the iteration law as early as Ref. [128]. The novelty in recent IIC is the use of the noncausal inverse G^{-1} in the iteration law [27,124]. In particular, at the k th iteration step, the input is

$$V_{\text{ff},k}(j\omega) = V_{\text{ff},k-1}(j\omega) + \rho(j\omega)G^{-1}(j\omega)[P_d(j\omega) - P_{k-1}(j\omega)] \quad (53)$$

where $k \geq 1$, $V_{\text{ff},0}(j\omega)$ is the initial input, $\rho(j\omega) \in \mathfrak{R}$ is the frequency-dependent iteration-gain, and $[P_d(j\omega) - P_{k-1}(j\omega)]$ represents the positioning error at the previous ($k-1$)th iteration step. Convergence of such procedures was studied in Refs. [27,124,129]. In particular, a frequency domain criterion was studied in Ref. [27], which showed that the IIC procedure converges at a frequency ω provided the phase error in the model is less than $\pi/2$, and the update gain $\rho(j\omega)$ is sufficiently small, i.e.,

$$0 \leq \rho(j\omega) < \frac{2 \cos(\Delta_\phi(j\omega))}{\Delta_M(j\omega)} \quad \text{and} \quad \Delta_\phi < \pi/2 \quad (54)$$

where Δ_M is the magnitude uncertainty and Δ_ϕ is the phase uncertainty. Similar requirements on the phase being less than $\pi/2$ degree arise in time-domain approaches to prove convergence of IIC [129], as well as in repetitive control methods for periodic trajectories [94,96].

Remark 9. (Choosing the iteration-gain). The optimal inverse can be used to find the frequency-dependent iteration-gain $\rho(j\omega)$ in Eq. (53), which accommodates the model-uncertainty variation with frequency, by choosing $\rho(j\omega) = \rho_{\text{opt}}(j\omega)$ as in Remark 8, Eq. (39).

Remark 10. (Noncausality of the IIC input). If there is substantial uncertainty at higher frequencies, then the iteration-gain $\rho(j\omega)$ in Eq. (53) needs to be zero at those high frequencies to guarantee convergence, and, therefore, the IIC input (in Eq. (53)) is necessarily noncausal (even for a minimum-phase system G) as in Remark 5.

Model-less IIC. The convergence of the inversion-based iterative control (IIC) (Eq. (53)) is limited by the modeling error of the linear dynamics map G , particularly the phase. Such a modeling-related constraint can be alleviated by adaptively updating the dynamics model G along with the iteration. Toward this, the inverse G^{-1} of the dynamics used in the IIC algorithm (Eq. (53)) is obtained from the measured input-output data from the previous iteration step [61,90,126], i.e.,

$$G_k^{-1}(j\omega) \rightarrow \frac{V_{\text{ff},k-1}(j\omega)}{P_{k-1}(j\omega)} \quad (55)$$

provided $P_{k-1}(j\omega) \neq 0$. Moreover, since the confidence level in the above online identification process is high, the update gain ρ is chosen as 1. Then, the IIC algorithm (Eq. (53)) becomes [61,126]

$$\begin{aligned} V_{\text{ff},k}(j\omega) &= V_{\text{ff},k-1}(j\omega) + \frac{V_{\text{ff},k-1}(j\omega)}{P_{k-1}(j\omega)} [P_d(j\omega) - P_{k-1}(j\omega)] \\ &= \frac{V_{\text{ff},k-1}(j\omega)}{P_{k-1}(j\omega)} [P_d(j\omega)] \end{aligned} \quad (56)$$

provided $P_k(j\omega) \neq 0$ and $P_d(j\omega) \neq 0$ at frequency ω ; the input $V_{\text{ff},k}(j\omega) = 0$ otherwise. The approach has been shown to be effective even with an initial model $G=1$. When sensors are not available to measure the actual output P , the input-output data needed to find the model (in Eq. (55)) can be obtained (during the iteration process) by using an image-based approach [90,91]. The challenge is to prove convergence in the presence of noise and disturbances that affect the estimated models. Convergence issues are studied in Ref. [126]. When compared with IIC with a fixed nominal model, the identification of the model (during iterations) has demonstrated substantial improvement in the convergence rate for nanopositioning applications in Refs. [61,126].

4.5.2 Iterative Control to Correct for Nonlinearities. Iterative approaches can be used to reduce positioning errors due to hysteresis, as demonstrated for SPM in Refs. [8,127]. While linearization methods (e.g., shown in Fig. 6) do reduce the hysteresis effect, iterations can reduce the residual hysteresis further, especially, during large-range positioning. For example, the residual hysteresis can still be as large as 60 nm when the position changes by 4 μm as shown in Fig. 7.

Convergence in the presence of hysteresis. The major challenge is to demonstrate convergence of iterative algorithms in the presence of hysteresis. The difficulty in proving convergence arises due to branching effects, which prevent the iterative algorithm from predicting the direction in which the input needs to be changed based on a measured output error. This is similar to the phase uncertainty being larger than $\pi/2$ in traditional iterative control methods. To illustrate this loss in direction due to branching effects, consider a typical hysteresis (output (P) versus input

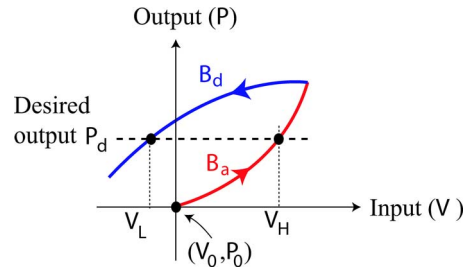


Fig. 14 Hysteresis curve with two branches: ascending B_a and descending B_d

(V) response shown in Fig. 14. For a desired output P_d , there are two possible input values, V_H on the ascending branch B_a and V_L on the descending branch B_d . Then given an input-output pair (V_0, P_0) and, therefore, the output error $P_d - P_0$, it is unclear if the input should be increased to V_H or decreased to V_L —unless it is known that the system is on the ascending branch. Therefore, convergence is established branch by branch as shown in Refs. [8,67,130] for iterative procedures of the form

$$V_{\text{ff},k}(t) = V_{\text{ff},k-1}(t) + \rho_{H1} [P_d(t) - P(t)] \quad (57)$$

Inverse-hysteresis iterative control. In addition to branching effects, the convergence of iterative approaches is also affected by the nonlinearity of the hysteresis. If the nonlinearity is not accounted for as in Refs. [8,130], then the iteration-gains need to be substantially small to enable convergence. Recent work [131] includes an inverse hysteresis operator H^{-1} in the iteration procedure, as

$$V_{\text{ff},k}(t) = V_{\text{ff},k-1}(t) + \rho_{H2} \{H^{-1}[P_d(\cdot)](t) - H^{-1}[P(\cdot)](t)\} \quad (58)$$

Convergence issues are studied in Ref. [131] to show that inverting the hysteresis nonlinearity can substantially improve the convergence rate of iterative algorithms. Moreover, this approach was used to improve lateral positioning precision and, thereby, feature accuracy in AFM-based nanofabrication in Ref. [131].

4.5.3 Application of IIC to SPM. IIC yields the highest precision in SPM positioning because of its ability to correct for modeling errors. For example, reduction of positioning error close to the sensor noise level was demonstrated in Refs. [27,61,126]. This high precision makes IIC attractive for repetitive SPM-probe positioning, in applications where precision is critical to performance. For example, IIC was used to reduce dynamics-coupling-caused errors in the desired AFM probe-sample force [27], to enable AFM measurements of the fast, rate-dependent elastic modulus of soft polymers in Ref. [132], and for rapid measurements of the adhesion force on a silicon sample in Ref. [133].

5 Research Directions in Feedforward Control

The use of feedforward in three current research efforts: (a) SPM-based nanoscale combinatorial-science studies, (b) imaging of large soft samples, and (c) image-based control for sensor-less SPM, are described below.

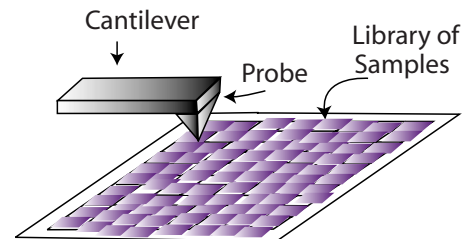


Fig. 15 Schematic of nanoscale combinatorial science: screening a library of samples with an AFM probe

5.1 Nanoscale Combinatorial-Science Studies. In combinatorial-science studies numerous combinations of samples are created and tested [134–136]. Integrating SPMs (e.g., an AFM as illustrated in Fig. 15) with combinatorial science allows this paradigm to be applied for molecular- and atomic-level studies. Increasing the SPM operating speed is necessary to increase the screening throughput of such libraries of samples. This requires both (a) high-speed SPM measurements of each sample, which require high-bandwidth vertical control; and (b) high-speed transitions of the SPM-probe from one sample to the next, which require high-bandwidth lateral control.

5.1.1 High-Speed Sample Property Measurements. High-bandwidth vertical control is needed to measure rapidly the properties of each sample in the library. For example, material properties (such as adhesion, friction, or bonding strength) at the nanoscale can be obtained from measurements of the interaction force between an AFM probe and the sample [137]. Since material properties are rate (and indentation time-profile) dependent, the probe-sample force needs to be measured by following specified sample-indentation curves. To avoid vibration-caused deviation from the specified sample-indentation curve during high-rate measurements, there is a need for high-bandwidth, precision, vertical positioning. Recent works have shown that inversion-based iterative control can be used to increase the indentation rate during sample property measurements. For example, IIC was used to enable AFM measurements of the fast, rate-dependent elastic modulus of soft polymers in Refs. [132,138].

5.1.2 High-Bandwidth Lateral Sample-to-Sample Control. High-bandwidth lateral control is necessary to move rapidly the SPM-probe from one sample to another, without residual vibrations when measuring properties at each sample. Since the time spent in this transition from one sample to another cannot be used for active measurements, the goal is to minimize this transition time for increasing throughput. It is, however, important to reduce (if not completely remove) residual positioning vibrations once the AFM probe has reached the next sampling position. This is an output transition problem, i.e., given an initial state $x(0)$ of the piezoscanner, the goal is to bring the output (lateral deflection, say, y) to a desired value $y(t_f)=\bar{y}$ and hold it constant afterwards, $t > t_f$. Previous works have shown that the integration of inversion and optimal control methods can lead to feedforward inputs that enable rapid output transitions without residual vibrations [64,139,140]. Such methods can be adapted to design fast sample-to-sample transitions in AFM-based combinatorial-science studies.

5.2 Imaging Large Soft Samples in Liquid. Imaging of cellular features requires SPM scan dimensions in the range 20–100 μm [141]. For example, the imaging of cell protrusions such as lamellipodia can require scan sizes in the order of 20 μm (see Refs. [142,143]). However, current AFM systems are too slow to investigate nanoscale variations in shape and volume of cellular processes with relatively large features, especially when imaging soft cells (without stiff cell walls) such as human cells [144,145]. Feedforward methods play an important role in the development of high-speed SPM for rapidly imaging such soft samples.

5.2.1 Scan Frequency Versus Scan Size for Soft Samples. For the same scan size, achieved scan frequencies for soft samples in liquid [43,47,53–57] tend to be several orders of magnitude lower than the scan frequencies achieved in air as compared in Fig. 5. This reduction in scan frequency is because of the need to maintain small probe-sample forces (i.e., high precision vertical positioning) to avoid damaging soft samples as opposed to hard samples [39,146]. For example, keeping the maximum force F_{max} below 0.1 nN when imaging soft cells [145] using AFM cantilevers with low stiffness (K_s around 0.01 N/m) requires positioning

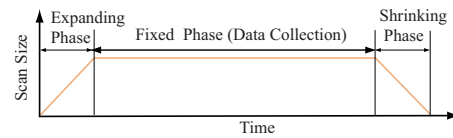


Fig. 16 Zoom approach [148,149]: the three scanning phases (expanding zoom-out phase, fixed phase, and shrinking zoom-in phase) to maintain small tip-sample forces during the iteration process

precision of $F_{\text{max}}/K_s=10$ nm or less. Variations in the sample's vertical features of more than 1 μm (which is typical in large soft cells) translates to a positioning precision of less than 0.1% of the positioning range, which is challenging to achieve at high operating speeds.

5.2.2 Development of Feedforward Vertical Control for Unknown Samples. Feedforward control is not readily applied to vertical positioning because the sample profile is not known a priori. For nonminimum-phase positioning systems, the noncausal, exact-inversion-based feedforward schemes, even those implemented in the time domain, require some prior knowledge of the scan path. The stringent precision requirement in the vertical direction favors the use of iterative methods, which can achieve precision close to the sensor noise levels—provided the iterations converge and the soft sample is not damaged during the iteration procedure.

5.2.3 The Problem of Large Forces During Iteration Procedure. The problem, with using iterative approaches, is to avoid large tip-sample forces as the iterative procedure converges—in particular, during the very first step in the iteration process. At the start of the iteration, the sample profile is unknown; therefore, it is difficult to use the inversion method to achieve SPM-probe positioning over the sample profile. This can lead to large tip-sample forces and sample damage at the very first iteration. One approach, to avoid such sample damage, is to use a slow scan for identifying the sample profile at the start of the iteration process and then use the inversion procedure to find the feedforward input for faster scans. The problem is that this slow scan can take a very long time. Moreover, the sample profile could change and the slow-scan image can be distorted by drift effects.

5.2.4 The Zoom Approach to IIC for Vertical Positioning. In SPM imaging applications, information from the previous scan line can be used to improve the positioning in the current scan line [147]. The main idea is that the current scan profile is close to the previous scan profile and, therefore, the positioning precision can be improved by using information from the previous scan line to develop the feedforward input for the current scan line. The challenge is to avoid large forces in the first iteration step, which can be accomplished by the zoom-out/zoom-in iterative approach [148,149]. This iterative approach has three phases as shown in Fig. 16: (a) Start with a small scan area and expand gradually, (b) fix the scan size at the desired value and image the sample, and (c) reduce the scan size to a small value.

The zoom approach achieves small tip-sample forces because of the small scan size at the start of the iterations. Note that sample-profile variations (with a small scan size) are small in the first iteration step. Therefore, the resulting positioning errors and the tip-sample forces are also small. The rate at which the scan size is changed during the expansion and reduction phases is adjusted to ensure that the variations in the tip-sample force are small.

The zoom approach was implemented to image relatively large soft samples in a liquid medium, in particular, to image soft hydrogel contact lenses in a saline solution using an AFM [148,149]. The zoom approach enabled imaging at higher scan frequencies—at 30 Hz over a 10×10 μm^2 scan area. This repre-

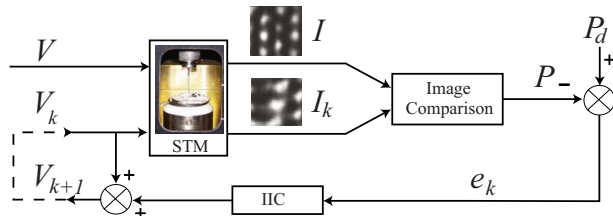


Fig. 17 Block diagram of image-based SPM control method [90]. At each iteration step, k , the SPM (in this case a STM) is used to acquire a low-speed and a high-speed image (I and I_k , respectively). These two images are compared with to determine the positioning error e_k , which is used by the IIC algorithm to determine the input V_{k+1} for the next iteration step to improve the SPM's positioning accuracy.

sents about an order of magnitude increase in the scan frequency (with the use of the zoom-based approach), when compared with previous results (see Fig. 5), for such large, soft samples in liquid.

5.3 Image-Based Control for Subnanometer-Scale Studies.

SPMs can achieve subnanometer-scale positioning, e.g., carbon atoms separated by 0.25 nm on a graphite surface can be imaged using a STM. However, the bandwidth at which STMs can achieve accurate subnanometer-scale positioning is limited by the inability to measure the position of the STM-probe's tip at high scan frequencies. For example, the resolution of external sensors (during high-frequency scanning) is limited due to sensor noise, which tends to increase with the scan frequency and temperature [150]. Moreover, standard external sensors cannot directly measure the lateral position of a STM-probe's atomically sharp tip. Instead external sensors can only measure the position of a different point on the STM scanner; the position of the STM-probe's tip can only be inferred from such measurements. (In contrast, the vertical position of the STM-probe's tip can be measured using the extant tunneling current sensor.) Thus, sensor deficiencies preclude the use of standard feedback control techniques when high-bandwidth lateral positioning is required at subnanometer scales. To enable high-bandwidth subnanometer-scale lateral positioning, an image-based control methodology has been developed that exploits the STM's extant imaging capabilities [90,91].

5.3.1 Image-Based Control. To resolve the problems associated with using external sensors, an iterative image-based feedforward control method has been developed to increase subnanometer-scale positioning bandwidth in Refs. [90,91]. This approach, which uses the image-distortion to model and compensate for dynamic effects, extends previously developed methods that have used SPM-images to correct for positioning errors caused at low operating speeds [151,152]. A block diagram of this image-based method is shown in Fig. 17.

The main idea is to quantify the error in positioning the SPM-

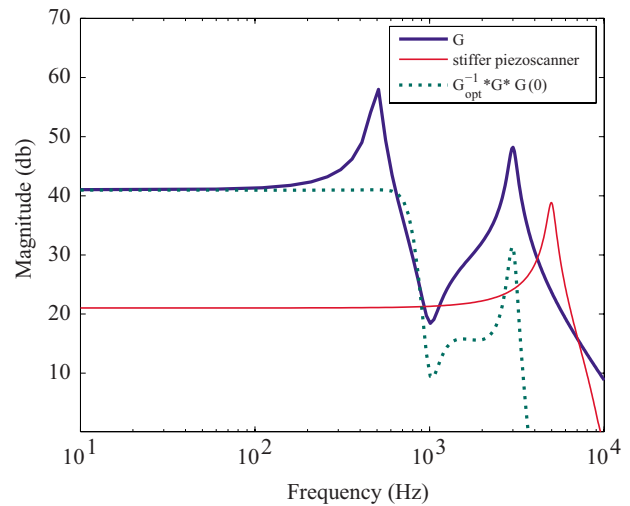


Fig. 19 Two approaches to increase positioning bandwidth of piezoscanner, where the system model is G in Eq. (8). (a) Flattening the frequency response by using the optimal inverse as feedforward (G_{opt}^{-1} in Sec. 4.4.2 with dc-gain $G(0)$ as in Eq. (9)). (b) Stiffening the system by increasing each resonant-vibrational frequency ω_z , ω_{p1} , and ω_{p2} and the gain k of G (in Eq. (8)) by an order of magnitude.

probe over the sample surface by using SPM-images of standard calibration samples. As the calibration sample surface is fixed (i.e., features do not vary), the distortion in the image can be used to quantify the positioning errors, model the dynamics using the input-output data [91], and correct the feedforward input to the SPM [90] using inversion-based iterative control. This method has been applied to control a STM during subnanometer-scale imaging as seen in Fig. 18. A low-speed image, where accurate positioning has been achieved, is shown in Fig. 18(a), where the hexagonal lattice structure and normal atomic separation typical of the imaged HOPG surface are visible. As the scan frequency is increased, positioning accuracy is lost resulting in a distorted image as seen in Fig. 18(b). With the use of the image-based control, in Fig. 18(c), high-bandwidth nanopositioning is achieved—note that the hexagonal lattice structure and normal atomic separation have been regained. This achieved high-frequency scan at 2 kHz (which was a data-collection-hardware limit in Ref. [91]), with the image-based feedforward approach, is approximately 60% of the lowest resonant-vibrational frequency of the system at 3 kHz, which is more than six times the typical 1/10 limit in Fig. 4.

6 Summary of Discussions

The previous discussions on feedforward approaches are summarized in this section along with concluding remarks.

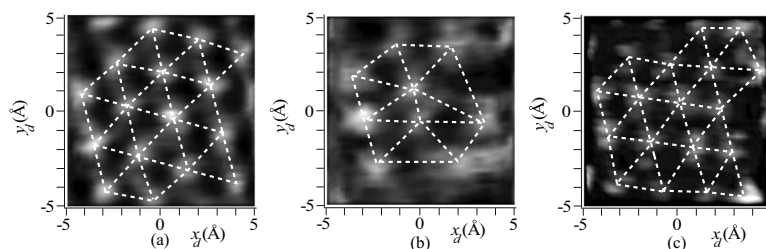


Fig. 18 Image-based control has been applied to enable high-speed imaging of a HOPG sample in Refs. [90,91]. (a) Accurate low-speed (100 Hz) STM image of graphite. (b) High-speed (2 kHz) STM image of the same graphite surface showing the distortion caused by positioning error. (c) High-speed (2 kHz) STM image obtained using image-based control [91].

Table 2 Highest precision feedforward techniques for SPM-probe positioning

	Known trajectory	Unknown trajectory
Repetitive	RC (Sec. 4.3.3) and IIC (Sec. 4.5) Advantage: correct error from uncertainty Application: periodic scanning (lateral) and repetitive nanofabrication (vertical) Research issue: convergence	Zoom approach, Sec. 5.2.4 Advantage: track unknown sample profile Application: imaging soft samples in liquid (vertical) Research issue: convergence
Nonrepetitive	Optimal inverse, Sec. 4.4.1 Advantage: account for model uncertainty Application: nonraster scanning (lateral) Research issue: model identification to improve performance	Exact inverse, Sec. 4.3.4 (minimum-phase) Advantage: improvement over feedback alone Application: nanofabrication (vertical) Research issues: performance limits under uncertainty and nonminimum-phase dynamics

6.1 Increasing SPM Speed. Two current approaches to increase the operation speed of SPMs are (a) suppressing the vibration (i.e., flattening the frequency response) using control such as the feedforward approach discussed in this article, and (b) increasing the lowest resonant-vibrational frequency by using stiffer actuators; these approaches are compared in Fig. 19. As discussed in Sec. 3.3, increasing the lowest resonant-vibrational frequency by an order of magnitude also tends to decrease the positioning range by an order of magnitude since they are inversely related (see Eq. (3)). In contrast, control methods such as using the optimal inverse as feedforward (see Sec. 4.4.1) can increase the operating speed without loss of positioning range. Moreover, these control methods can be used to suppress vibrations and, thereby, increase the operating speed of SPMs with stiffer actuators.

6.2 Applicability of Feedforward to SPM-Probe Positioning. SPM-probe positioning can be broadly classified into two types: lateral and vertical as discussed in Sec. 2.3. In each type the applicability of the different types of feedforward methods depends on whether (a) the positioning can be considered to be repetitive (in which case iterative methods can improve positioning performance) or nonrepetitive, and (b) the position trajectory is known or unknown. The approach that yields the highest precision for each of these cases is presented in Table 2, along with example SPM application as well as the main research issues.

6.3 Emerging Research Problems. Emerging SPM developments include the development of multistage positioning designs to increase both range and precision, e.g., the use of active SPM-probes [153], as well as multiple-probe SPMs [19] to increase the overall throughput. These systems will add to control issues, such as the need (a) to exploit actuator redundancy in multistage designs, (b) to identify the dynamics of large arrays of SPM-probes, and (c) to implement highly parallel control schemes. Additionally, the high-bandwidth, nanopositioning problem in SPM can benefit from the application of existing control methods available for vibration suppression in the fast positioning of general flexible structures, which has been well studied in literature.

Acknowledgment

The authors thank co-workers D. Croft and H. Perez for their contributions (as referenced in the article). The research was funded through NSF Grant Nos. CMS 0196214, CMS 0336221, CMII 0624597, CMII 0856091, and DUE 0632913, as well as NIH Grant No. GM068103. Additionally, S.D. is grateful for the support from the National Science Council of Taiwan (Republic of China), Grant No. NSC 96-2221-E-006-245, for a sabbatical visit to the National Cheng Kung University, Tainan, Taiwan.

References

- [1] Binnig, G., and Rohrer, H., 1982, "Scanning Tunneling Microscopy," *Helv. Phys. Acta*, **55**, pp. 726–735.
- [2] Binnig, G., Quate, C. F., and Gerber, C., 1986, "Atomic Force Microscope,"

- Phys. Rev. Lett.*, **56**(9), pp. 930–933.
- [3] 1994, *Scanning Probe Microscopy and Spectroscopy*, R. Wiesendanger, ed., Cambridge University Press, Cambridge.
- [4] Vettiger, P., Stauffer, U., and Kern, D. P., 1996, "Special Issue on Nanotechnology—Preface," *Microelectron. Eng.*, **31**, pp. 1–2.
- [5] Gentili, M., Giovannella, C., and Selci, S., eds. 1993, "Nanolithography: A Borderland Between STM, EB, IB and X-Ray Lithographies," NATO ASI Series E: Applied Science, Vol. 264, Kluwer Academic Publishers.
- [6] Whitesides, G. M., and Love, H. C., 2001, "The Art of Building Small," *Sci. Am.*, **285**(3), pp. 39–47.
- [7] Kalinin, S. V., and Bonnell, D. A., 2000, "Effect of Phase Transition on the Surface Potential of the BaTiO₃," *J. Appl. Phys.*, **87**(8), pp. 3950–3957.
- [8] Leang, K. K., and Devasia, S., 2006, "Design of Hysteresis-Compensating Iterative Learning Control: Application to Atomic Force Microscopes," *Mechatronics*, **16**(3–4), pp. 141–158.
- [9] Bashash, S., and Jalili, N., 2008, "A Polynomial-Based Linear Mapping Strategy for Feedforward Compensation of Hysteresis in Piezoelectric Actuators," *ASME J. Dyn. Syst., Meas., Control*, **130**(3), p. 031008.
- [10] Barrett, R. C., and Quate, C. F., 1991, "Optical Scan-Correction System Applied to Atomic Force Microscopy," *Rev. Sci. Instrum.*, **62**(6), pp. 1393–1399.
- [11] Devasia, S., Eleftheriou, E., and Moheimani, S. O. R., 2007, "A Survey of Control Issues in Nanopositioning," *IEEE Trans. Control Syst. Technol.*, **15**(5), pp. 802–823.
- [12] Croft, D., and Devasia, S., 1999, "Vibration Compensation for High Speed Scanning Tunneling Microscopy," *Rev. Sci. Instrum.*, **70**(12), pp. 4600–4605.
- [13] Alexander, S., Hellemans, L., Marti, O., Schneir, J., Elings, V., Hansma, P. K., Longmire, M., and Gurley, J., 1989, "An Atomic-Resolution Atomic-Force Microscope Implemented Using an Optical Lever," *J. Appl. Phys.*, **65**(1), pp. 164–167.
- [14] Pearce, R., and Vancso, G. J., 1998, "Real-Time Imaging of Melting and Crystallization in Poly(Ethylene Oxide) by Atomic Force Microscopy," *Polymer*, **39**(5), pp. 1237–1242.
- [15] Li, L., Chan, C.-M., Yeung, K. L., Li, J.-X., Ng, K.-M., and Lei, Y., 2001, "Direct Observation of Growth of Lamellae and Spherulites of a Semicrystalline Polymer by AFM," *Macromolecules*, **34**(2), pp. 316–325.
- [16] Beekmans, L. G. M., van der Meer, D. W., and Vancso, G. J., 2002, "Crystal Melting and Its Kinetics on Poly(Ethylene Oxide) by In Situ Atomic Force Microscopy," *Polymer*, **43**(6), pp. 1887–1895.
- [17] Evans, E., and Ritchie, K., 1997, "Dynamic Strength of Molecular Adhesion Bonds," *Biophys. J.*, **72**(4), pp. 1541–1555.
- [18] Stipe, B. C., Rezaei, M. A., and Ho, W., 1998, "Single-Molecule Vibrational Spectroscopy," *Science*, **280**, pp. 1732–1735.
- [19] Wilder, K., Soh, H. T., Atalar, A., and Quate, C. F., 1999, "Nanometer-Scale Patterning and Individual Current Controlled Lithography Using Multiple Scanning Probes," *Rev. Sci. Instrum.*, **70**, pp. 2822–2827.
- [20] Minne, S. C., Yaraliuglu, G., Manalis, S. R., Adams, J. D., Zesch, J., Atalar, A., and Quate, C. F., 1998, "Automated Parallel High-Speed Atomic Force Microscopy," *Appl. Phys. Lett.*, **72**(18), pp. 2340–2342.
- [21] Lozanne, A. L. D., Smith, W. F., and Ehrlich, E. E., 1993, "Direct Writing With a Combined STM/SEM System," *Proceedings of NATO Advanced Workshop on Nanolithography: A Borderland between STM, EB, IB, and X-ray Lithographies*, NATO ASI Series E, Applied Science, Vol. 264, pp. 159–174.
- [22] Aizenberg, J., Black, A. J., and Whitesides, G. M., 1999, "Control of Crystal Nucleation by Patterned Self-Assembled Monolayers," *Nature (London)*, **398**, pp. 495–498.
- [23] Coffey, D. C., and Ginger, D. S., 2005, "Patterning Phase Separation in Polymer Films With Dip-Pen Nanolithography," *J. Am. Chem. Soc.*, **127**, pp. 4564–4565.
- [24] Chung, S. W., Ginger, D. S., Morales, M., Zhang, Z., Chandrasekhar, V., Ratner, M. A., and Mirkin, C. A., 2005, "Top-Down Meets Bottom-Up: Dip-Pen Nanolithography and DNA-Directed Assembly of Nanoscale Electrical Circuits," *Small*, **1**, pp. 64–69.
- [25] Park, C., Yoon, J., and Thomas, E. L., 2003, "Enabling Nanotechnology With Self Assembled Block Copolymer Patterns," *Polymer*, **44**(22), pp. 6725–6760.
- [26] Stark, R. W., Schitter, G., and Stemmer, A., 2004, "Velocity Dependent Friction Laws in Contact Mode Atomic Force Microscopy," *Ultramicroscopy*, **100**(3–4), pp. 309–317.

- [27] Tien, S., Zou, Q., and Devasia, S., 2005, "Iterative Control of Dynamics-Coupling-Caused Errors in Piezoscanners During High-Speed AFM Operation," *IEEE Trans. Control Syst. Technol.*, **13**(6), pp. 921–931.
- [28] Avouris, P., Hertel, T., and Martel, R., 1997, "Atomic Force Microscope Tip-Induced Local Oxidation of Silicon: Kinetics, Mechanism, and Nanofabrication," *Appl. Phys. Lett.*, **71**, pp. 285–287.
- [29] Dubois, E., and Bubendorff, J. L., 2000, "Kinetics of Scanned Probe Oxidation: Space-Charge Limited Growth," *J. Appl. Phys.*, **87**(11), pp. 8148–8154.
- [30] Croft, D., Shedd, G., and Devasia, S., 2001, "Creep, Hysteresis, and Vibration Compensation for Piezoactuators: Atomic Force Microscopy Application," *ASME J. Dyn. Syst., Meas., Control*, **123**(1), pp. 35–43.
- [31] Clayton, G. M., Tien, S., Fleming, A. J., Moheimani, S. O. R., and Devasia, S., 2008, "Inverse Feedforward of Charge Controlled Piezopositioners," *Mechatronics*, **18**(5–6), pp. 273–281.
- [32] Ashhab, M., Salapaka, M., Dahleh, M., and Mezic, I., 1999, "Melnikov-Based Dynamical Analysis of Microcantilevers in Scanning Probe Microscopy," *Nonlinear Dyn.*, **20**(3), pp. 197–220.
- [33] El Rifai, O. M., and Youcef-Toumi, K., 2001, "In-Contact Dynamics of Atomic Force Microscopes," *Proceedings of the 2001 IEEE/ASME International Conference on Advanced Intelligent Mechatronics*, Jul. 8–12, Vol. 2, pp. 1325–1328.
- [34] Basak, S., Raman, A., and Garimella, S. V., 2006, "Hydrodynamic Loading of Microcantilevers Vibrating in Viscous Fluids," *J. Appl. Phys.*, **99**, p. 114906.
- [35] El Rifai, O. M., and Youcef-Toumi, K., 2001, "Coupling in Piezoelectric Tube Scanners Used in Scanning Probe Microscopes," *Proceedings of the 2001 American Control Conference*, Arlington, VA, Jun. 25–27, Vol. 4, pp. 3251–3255.
- [36] Salapaka, S., De, T., and Sebastian, A., 2005, "Sample-Profile Estimate for Fast Atomic Force Microscopy," *Appl. Phys. Lett.*, **87**(5), p. 053112.
- [37] Shegaonkar, A. C., and Salapaka, S. M., 2007, "Feedback Based Simultaneous Correction of Imaging Artifacts Due to Geometrical and Mechanical Cross-Talk and Tip-Sample Stick in Atomic Force Microscopy," *Rev. Sci. Instrum.*, **78**, p. 103706.
- [38] Li, Y., and Bechhoefer, J., 2007, "Feedforward Control of a Closed-Loop Piezoelectric Translation Stage for Atomic Force Microscope," *Rev. Sci. Instrum.*, **78**(1), pp. 013702.
- [39] Barrett, R. C., and Quate, C. F., 1991, "High-Speed, Large-Scale Imaging With the Atomic Force Microscope," *J. Vac. Sci. Technol. B*, **9**(2), pp. 302–306.
- [40] Kuipers, L., Loos, R. W. M., Neerings, H., ter Horst, J., Ruwiel, G. J., de Jongh, A. P., and Frenken, J. W. M., 1995, "Design and Performance of a High Temperature, High-Speed Scanning Tunneling Microscope," *Rev. Sci. Instrum.*, **66**(9), pp. 4557–4565.
- [41] Nakakura, C. Y., Phanse, V. M., Zheng, G., Bannon, G., Altman, E. I., and Lee, K. P., 1998, "A High-Speed Variable-Temperature Ultrahigh Vacuum Scanning Tunneling Microscope," *Rev. Sci. Instrum.*, **69**(9), pp. 3251–3258.
- [42] Schitter, G., Aström, K. J., DeMartini, B. E., Thurner, P. J., Turner, K. L., and Hansma, P. K., 2007, "Design and Modeling of a High-Speed AFM-Scanner," *IEEE Trans. Control Syst. Technol.*, **15**(5), pp. 906–915.
- [43] Ando, T., Kodera, N., Takai, E., Maruyama, D., Saito, K., and Toda, A., 2001, "A High-Speed Atomic Force Microscope for Studying Biological Macromolecules," *Proc. Natl. Acad. Sci. U.S.A.*, **98**(22), pp. 12468–12472.
- [44] Rost, M. J., Crama, L., Schakel, P., Tol, E. V., Velzen-Williams, G. B. E. M. V., Overgaw, C. F., Horst, H. T., Dekker, H., Okhuijsen, B., Seynen, M., Vijftigchild, A., Han, P., Katan, A. J., Schoots, K., Schumm, R., Loo, W. V., Oosterkamp, T. H., and Frenken, J. W. M., 2005, "Scanning Probe Microscopes Go Video Rate and Beyond," *Rev. Sci. Instrum.*, **76**(5), p. 053710.
- [45] Shao, Z., Mou, J., Czajkowsky, D. M., Yang, J., and Yuan, J.-Y., 1996, "Biological Atomic Force Microscopy: What Is Achieved and What Is Needed," *Adv. Phys.*, **45**(1), pp. 1–86.
- [46] Viani, M. B., Schaffer, T. E., Chand, A., Rief, M., Gaub, H. E., and Hansma, P. K., 1999, "Small Cantilevers for Force Spectroscopy of Single Molecules," *J. Appl. Phys.*, **86**(4), pp. 2258–2262.
- [47] Viani, M. B., Schaffer, T. E., Paloczi, G. T., Pietrasanta, L. I., Smith, B. L., Thompson, J. B., Rief, M., Gaub, H. E., Plaxco, K. W., Cleland, A. N., Hansma, H. G., and Hansma, P. K., 1999, "Fast Imaging and Fast Force Spectroscopy of Single Biopolymers With a New Atomic Force Microscope Designed for Small Cantilever," *Rev. Sci. Instrum.*, **70**(11), pp. 4300–4303.
- [48] Koops, R., and Sawatzky, G. A., 1992, "New Scanning Device for Scanning Tunneling Microscope Applications," *Rev. Sci. Instrum.*, **63**(8), pp. 4008–4009.
- [49] Sulchek, T., Hsieh, R., Adams, J. D., Minne, S. C., Quate, C. F., and Adderton, D. M., 2000, "High-Speed Atomic Force Microscopy in Liquid," *Rev. Sci. Instrum.*, **71**(5), pp. 2097–2099.
- [50] Chen, C. J., 1992, "Electromechanical Deflections of Piezoelectric Tubes With Quartered Electrodes," *Appl. Phys. Lett.*, **60**(1), pp. 132–134.
- [51] Humphris, A., Miles, M., and Hobbs, J., Jan, 2005, "A Mechanical Microscope: High-Speed Atomic Force Microscopy," *Appl. Phys. Lett.*, **86**(3), p. 034106.
- [52] Picco, L. M., Bozec, L., Ulcinas, A., Engledew, D. J., Antognozzi, M., Horton, M. A., and Miles, M. J., 2007, "Breaking the Speed Limit With Atomic Force Microscopy," *Nanotechnology*, **18**(4), p. 044030.
- [53] Uchihashi, T., Ando, T., and Yamashita, H., 2006, "Fast Phase Imaging in Liquids Using a Rapid Scan Atomic Force Microscope," *Appl. Phys. Lett.*, **89**(21), pp. 213112.
- [54] De Cupere, V. M., Wetter, J. V., and Rouxhet, P. G., 2003, "Nanoscale Organization of Collagen and Mixed Collagen-Pluronic Adsorbed Layers," *Langmuir*, **19**, pp. 6957–6967.
- [55] Jiao, Y., and Schäffer, T. E., 2004, "Accurate Height and Volume Measurements on Soft Samples With the Atomic Force Microscope," *Langmuir*, **20**, pp. 10038–10045.
- [56] Dong, H., Wanyun, M., Fulong, L., Meiling, Y., Zhigang, O., and Yunxu, S., 2003, "Time-Series Observation of the Spreading Out of Microvessel Endothelial Cells With Atomic Force Microscopy," *Phys. Med. Biol.*, **48**, pp. 3897–3909.
- [57] Ushiki, T., Yamamoto, S., Hitomi, J., Ogura, S., Umemoto, T., and Shigeno, M., 2000, "Atomic Force Microscopy of Living Cells," *Jpn. J. Appl. Phys., Part 1*, **39**(6B), pp. 3761–3764.
- [58] Salapaka, S., Sebastian, A., Cleveland, J. P., and Salapaka, M. V., 2002, "High Bandwidth Nano-Positioner: A Robust Control Approach," *Rev. Sci. Instrum.*, **73**(9), pp. 3232–3241.
- [59] Ando, Y., Ikehara, T., and Matsumoto, S., 2007, "Development of Three-Dimensional Microstages Using Inclined Deep-Reactive Ion Etching," *J. Microelectromech. Syst.*, **16**(3), pp. 613–621.
- [60] Leang, K. K., and Fleming, A. J., 2008, "High-Speed Serial-Kinematic AFM Scanner: Design and Drive Considerations," *Proceedings of the American Control Conference*, Seattle, WA, Jun. 11–13, pp. 3188–3193.
- [61] Li, Y., and Bechhoefer, J., 2008, "Feedforward Control of a Piezoelectric Flexure Stage for AFM," *Proceedings of the American Control Conference*, Seattle, WA, Jun. 11–13, pp. 2703–2709.
- [62] Yong, Y. K., Aphale, S. S., and Reza Moheimani, S. O., 2009, "Design, Identification, and Control of a Flexure-Based xy Stage for Fast Nanoscale Positioning," *IEEE Trans. Nanotechnol.*, **8**(1), pp. 46–54.
- [63] Schitter, G., Thurner, P. J., and Hansma, P. K., 2008, "Design and Input-Shaping Control of a Novel Scanner for High-Speed Atomic Force Microscopy," *Mechatronics*, **18**(5–6), pp. 282–288.
- [64] Perez, H., Zou, Q., and Devasia, S., 2004, "Design and Control of Optimal Scan-Trajectories: Scanning Tunneling Microscope Example," *ASME J. Dyn. Syst., Meas., Control*, **126**(1), pp. 187–197.
- [65] Fleming, A. J., and Wills, A., 2008, "Optimal Input Signals for Bandlimited Scanning Systems," *Proceedings of the 17th IFAC World Congress*, Seoul, Korea, Jul. 6–11, pp. 11805–11810.
- [66] Mokaberli, B., and Requicha, A. A. G., 2008, "Compensation of Scanner Creep and Hysteresis for AFM Nanomanipulation," *IEEE Trans. Autom. Sci. Eng.*, **5**(2), pp. 197–206.
- [67] Tan, X., and Iyer, R. V., 2009, "Modeling and Control of Hysteresis," *IEEE Control Syst. Mag.*, **29**, pp. 26–29.
- [68] Okazaki, Y., 1990, "A Micro-Positioning Tool Post Using a Piezoelectric Actuator for Diamond Turning Machines," *Precis. Eng.*, **12**, pp. 151–156.
- [69] Leang, K., and Devasia, S., 2002, "Hysteresis, Creep, and Vibration Compensation for Piezoactuators: Feedback and Feedforward Control," *Proceedings of the Second IFAC Conference on Mechatronic Systems*, Berkeley, CA, Dec. 9–11, pp. 283–289.
- [70] Comstock, R., 1981, "Charge Control of Piezoelectric Actuators to Reduce Hysteresis Effect," U.S. Patent No. 4,263,527.
- [71] Newcomb, C. V., and Flinn, I., 1982, "Improving the Linearity of Piezoelectric Ceramic Actuators," *Electron. Lett.*, **18**(11), pp. 442–444.
- [72] Fleming, A. J., and Moheimani, S. O. R., 2005, "A Grounded-Load Charge Amplifier for Reducing Hysteresis in Piezoelectric Tube Scanners," *Rev. Sci. Instrum.*, **76**(7), p. 073707.
- [73] Fleming, A. J., and Leang, K. K., 2008, "Charge Drives for Scanning Probe Microscope Positioning Stages," *Ultramicroscopy*, **108**, pp. 1551–1557.
- [74] Sebastian, A., and Salapaka, S., 2005, "Design Methodologies for Robust Nano-Positioning," *IEEE Trans. Control Syst. Technol.*, **13**(6), pp. 868–876.
- [75] Tamer, N., and Dahleh, M. A., 1994, "Feedback Control of Piezoelectric Tube Scanners," *Proceedings of the Control and Decision Conference*, Lake Buena Vista, FL, pp. 1826–1831.
- [76] Daniele, A., Salapaka, S., Salapaka, M., and Dahleh, M., 1999, "Piezoelectric Scanners for Atomic Force Microscopes: Design of Lateral Sensors, Identification and Control," *Proceedings of the American Control Conference*, San Diego, CA, pp. 253–257.
- [77] Schitter, G., Menold, P., Knapp, H. F., Allgower, F., and Stemmer, A., 2001, "High Performance Feedback for Fast Scanning Atomic Force Microscopy," *Rev. Sci. Instrum.*, **72**(8), pp. 3320–3327.
- [78] Salapaka, M. V., 2008, "Systems and Control Approaches to Nano-Interrogation: Unraveling New Temporal and Spatial Regimes," keynote paper, Invited Session on Dynamics and Control of Micro- and Nanoscale Systems-III, IFAC World Congress.
- [79] Salapaka, S. M., and Salapaka, M. V., 2008, "Scanning Probe Microscopy," *IEEE Control Syst. Mag.*, **28**(2), pp. 65–83.
- [80] Pao, L. Y., Butterworth, J. A., and Abramovitch, D. Y., 2007, "Combined Feedforward/Feedback Control of Atomic Force Microscopes," *Proceedings of the 2007 American Control Conference*, New York, NY, Jul. 11–13, pp. 3509–3515.
- [81] Butterworth, J. A., Pao, L. Y., and Abramovitch, D. Y., 2008, "A Comparison of Control Architectures for Atomic Force Microscopes," *Proceedings of the IFAC World Congress*, Seoul, Korea, Jul., pp. 8236–8250.
- [82] Leang, K. K., and Devasia, S., 2007, "Feedback-Linearized Inverse Feedforward for Creep, Hysteresis, and Vibration Compensation in AFM Piezoactuators," *IEEE Trans. Control Syst. Technol.*, **15**(5), pp. 927–935.
- [83] Aphale, S. S., Devasia, S., and Moheimani, S. O. R., 2008, "High-Bandwidth Control of a Piezoelectric Nanopositioning Stage in the Presence of Plant Uncertainties," *Nanotechnology*, **19**(12), p. 125503.
- [84] Zou, Q., Leang, K. K., Sadoun, E., Reed, M. J., and Devasia, S., 2004, "Control Issues in High-Speed AFM for Biological Applications: Collagen Imaging

- Example," *Asian J. Control*, **6**(2), pp. 164–178.
- [85] Zhao, Y., and Jayasuriya, S., 1995, "Feedforward Controllers and Tracking Accuracy in the Presence of Plant Uncertainties," *ASME J. Dyn. Syst., Meas., Control*, **117**, pp. 490–495.
- [86] Schitter, G., Stemmer, A., and Allgower, F., 2003, "Robust 2dof-Control of a Piezoelectric Tube Scanner for High-Speed Atomic Force Microscopy," *Proceedings of the American Control Conference*, Denver, CO, pp. 3720–3725.
- [87] Ying, W., and Zou, Q., 2007, "Robust-Inversion-Based 2DOF-Control Design for Output Tracking: Piezoelectric Actuator Example," *IEEE Conference on Decision and Controls*, New Orleans, LA, Dec., pp. 2451–2457.
- [88] Morgan Matroc, I., 1997, *Guide to Modern Piezoelectric Ceramics*, Rev. 7-91, Morgan Matroc, Inc., Bedford, OH.
- [89] Isidori, A., 1989, *Nonlinear Control Systems: An Introduction*, Springer-Verlag, Berlin.
- [90] Clayton, G. M., and Devasia, S., 2005, "Image-Based Control of Dynamic Effects in Scanning Tunneling Microscopes," *Nanotechnology*, **16**(6), pp. 809–818.
- [91] Clayton, G. M., and Devasia, S., 2007, "Iterative Image-Based Modeling and Control for Higher Scanning Probe Microscope Performance," *Rev. Sci. Instrum.*, **78**(8), p. 083704.
- [92] Inoue, T., Nakano, M., and Lwai, S., 1981, "High Accuracy Control of a Proton Synchrotron Magnet Power Supply," *Proceedings of the Eighth IFAC World Congress*, pp. 216–221.
- [93] Tomizuka, M., Tsao, T. C., and Chew, K. K., 1988, "Discrete Time Domain Analysis and Synthesis of Repetitive Controllers," *Proceedings of the American Control Conference*, pp. 860–866.
- [94] Ghosh, J., and Paden, B., 2000, "Nonlinear Repetitive Control," *IEEE Trans. Autom. Control*, **45**(5), pp. 949–954.
- [95] Francis, B., and Wonham, W. M., 1976, "The Internal Model Principle of Control Theory," *Automatica*, **12**(5), pp. 457–465.
- [96] Aridogan, U., Shan, Y., and Leang, K. K., 2008, "Discrete-Time Phase Compensated Repetitive Control for Piezoactuators in Scanning Probe Microscopes," *Dynamic Systems and Controls Conference*, Ann Harbor, MI, Paper No. DSCC2008-2283, pp. 1325–1332.
- [97] Aridogan, U., Shan, Y., and Leang, K. K., 2009, "Design and Analysis of Discrete-Time Repetitive Control for Scanning Probe Microscopes," *ASME J. Dyn. Syst., Meas., Control*, in press.
- [98] Silverman, L. M., 1969, "Inversion of Multivariable Linear Systems," *IEEE Trans. Autom. Control*, **14**(3), pp. 270–276.
- [99] Bayo, E., 1987, "A Finite-Element Approach to Control the End-Point Motion of a Single-Link Flexible Robot," *J. Rob. Syst.*, **4**(1), pp. 63–75.
- [100] Kwon, D., and Book, W. J., 1994, "A Time-Domain Inverse Dynamic Tracking Control of a Single-Link Flexible Manipulator," *ASME J. Dyn. Syst., Meas., Control*, **116**(2), pp. 193–200.
- [101] Devasia, S., Chen, D., and Paden, B., 1996, "Nonlinear Inversion-Based Output Tracking," *IEEE Trans. Autom. Control*, **41**(7), pp. 930–943.
- [102] Zou, Q., and Devasia, S., 1999, "Preview-Based Stable-Inversion for Output Tracking," *ASME J. Dyn. Syst., Meas., Control*, **121**(4), pp. 625–630.
- [103] Andersson, S. B., and Park, J., 2005, "Tip Steering for Fast Imaging in AFM," *Proceedings of the American Control Conference*, Portland, OR, Jun. 8–10, Vol. 4, pp. 2469–2474.
- [104] Zou, Q., and Devasia, S., 2004, "Preview-Based Optimal Inversion for Output Tracking: Application to Scanning Tunneling Microscopy," *IEEE Trans. Control Syst. Technol.*, **12**(3), pp. 375–386.
- [105] Tomizuka, M., and Whitney, D. E., 1975, "Optimal Discrete Finite Preview Problems (Why and How Is Future Information Important)," *ASME J. Dyn. Syst., Meas., Control*, **109**, pp. 319–325.
- [106] Zou, Q., 2009, "Optimal Preview-Based Stable-Inversion for Output Tracking of Nonminimum-Phase Linear Systems," *Automatica*, **45**(1), pp. 230–237.
- [107] Qui, L., and Davison, E. J., 1993, "Performance Limitations of Non-Minimum Phase Systems in the Servomechanism Problem," *Automatica*, **29**(March), pp. 337–349.
- [108] Francis, B., 1977, "The Linear Multivariable Regulator Problem," *SIAM J. Control Optim.*, **15**, pp. 486–505.
- [109] Tomizuka, M., 1987, "Zero Phase Error Tracking Control for Digital Control," *ASME J. Dyn. Syst., Meas., Control*, **109**, pp. 65–68.
- [110] Gopalswamy, S., and Hedrick, J., 1993, "Tracking Nonlinear Non-Minimum Phase Systems Using Sliding Control," *Int. J. Control*, **57**(5), pp. 1141–1158.
- [111] Devasia, S., 2002, "Should Model-Based Inverse Inputs Be Used as Feedforward Under Plant Uncertainty?," *IEEE Trans. Autom. Control*, **47**(11), pp. 1865–1871.
- [112] Dewey, J., Leang, K., and Devasia, S., 1998, "Experimental and Theoretical Results in Output-Trajectory Redesign for Flexible Structures," *ASME J. Dyn. Syst., Meas., Control*, **120**(4), pp. 456–461.
- [113] Gupta, N. K., 1980, "Frequency Shaped Cost Functionals: Extension of Linear-Quadratic-Gaussian Design Methods," *J. Guid. Control*, **3**(6), pp. 529–535.
- [114] Brinkerhoff, R., and Devasia, S., 2000, "Output Tracking for Actuator Deficient/Redundant Systems: Multiple Piezoactuator Example," *J. Guid. Control Dyn.*, **23**(2), pp. 370–373.
- [115] Schitter, G., Stark, R. W., and Stemmer, A., 2004, "Identification and Open-Loop Tracking Control of a Piezoelectric Tube Scanner for High-Speed Scanning-Probe Microscopy," *IEEE Trans. Control Syst. Technol.*, **12**(3), pp. 449–454.
- [116] Doyle, J. C., Francis, B. A., and Tannenbaum, A. R., 1992, *Feedback Control Theory*, Macmillan, London.
- [117] Arimoto, S., Kawamura, S., and Miyazaki, F., 1984, "On the Optimal Stabilization of Nonlinear Systems," *J. Rob. Syst.*, **1**(2), pp. 123–140.
- [118] Craig, J. J., 1984, "Adaptive Control of Manipulators Through Repeated Trials," *Proceedings of the American Control Conference*, pp. 1566–1573.
- [119] Moore, K. L., 1993, *Iterative Learning Control for Deterministic Systems*, Springer-Verlag, London.
- [120] Ghosh, J., and Paden, B., 2001, "Iterative Learning Control for Nonlinear Nonminimum Phase Plants," *ASME J. Dyn. Syst., Meas., Control*, **123**, pp. 21–30.
- [121] Mishra, S., and Tomizuka, M., 2005, "An Optimization-Based Approach for Design of Iterative Learning Controllers With Accelerated Rates of Convergence," *Proceedings of the 44th IEEE Conference on Decision and Control*, Seville, Spain, Dec. 12–15, Vol. 115, pp. 2427–2432.
- [122] Bristow, D., and Alleyne, A., 2008, "Monotonic Convergence of Iterative Learning Control for Uncertain Systems Using a Time-Varying Filter," *IEEE Trans. Autom. Control*, **53**(2), pp. 582–585.
- [123] Tsao, T., and Tomizuka, M., 1987, "Adaptive Zero Phase Error Tracking Algorithm for Digital Control," *ASME J. Dyn. Syst., Meas., Control*, **109**(2), pp. 349–354.
- [124] Ghosh, J., and Paden, B., 2002, "A Pseudo-Inverse Based Iterative Learning Control," *IEEE Trans. Autom. Control*, **47**(5), pp. 831–837.
- [125] Schitter, G., Stark, R. W., and Stemmer, A., 2004, "Fast Contact-Mode Atomic Force Microscopy on Biological Specimen by Model-Based Control," *Ultramicroscopy*, **100**(3–4), pp. 253–257.
- [126] Kim, K.-S., and Zou, Q., 2008, "Model-Less Inversion-Based Iterative Control for Output Tracking: Piezo Actuator Example," *Proceedings of the American Control Conference*, Seattle, WA, Jun. 11–13, pp. 2170–2175.
- [127] Wu, Y., and Zou, Q., 2007, "Iterative Control Approach to Compensate for Both the Hysteresis and the Dynamics Effects of Piezo Actuators," *IEEE Trans. Control Syst. Technol.*, **15**(5), pp. 936–944.
- [128] Atkeson, C. G., and McIntyre, J., 1986, "Robot Trajectory Learning Through Practice," *IEEE International Conference on Robotics and Automation*, pp. 1737–1742.
- [129] Ghosh, J., and Paden, B., 1999, "A Pseudo-Inverse Based Iterative Learning Control for Nonlinear Plants With Disturbances," *IEEE Conference on Decision and Control*, Dec.
- [130] Iyer, R., Tan, X., and Krishnaprasad, P., 2005, "Approximate Inversion of the Preisach Hysteresis Operator With Application to Control of Smart Actuators," *IEEE Trans. Autom. Control*, **50**(6), pp. 798–810.
- [131] Ashley, S. C., Aridogan, U., and Leang, K. K., 2008, "Hysteresis Inverse Iterative Learning Control of Piezoactuators in AFM," *17th IFAC World Congress*, Seoul, Korea.
- [132] Kim, K., Lin, Z., Shriotrya, P., Sundararajan, S., and Zou, Q., 2008, "Iterative Control Approach to High-Speed Force-Distance Curve Measurement Using AFM: Time Dependent Response of PDMS," *Ultramicroscopy*, **108**, pp. 911–920.
- [133] Kim, K., Zou, Q., and Su, C., 2008, "A New Approach to Scan-Trajectory Design and Track: AFM Force Measurement Example," *ASME J. Dyn. Syst., Meas., Control*, **130**, p. 051005.
- [134] Kassel, D. B., 2001, "Combinatorial Chemistry and Mass Spectrometry in the 21st Century Discovery Laboratory," *Chem. Rev. (Washington, D.C.)*, **101**, pp. 255–267.
- [135] Szostak, J., 1997, "Combinatorial Chemistry: Special Thematic Issue," *Chem. Rev. (Washington, D.C.)*, **97**, pp. 347–509.
- [136] Cawse, J. N., 2001, "Experimental Strategies for Combinatorial and High-Throughput Materials Development," *Acc. Chem. Res.*, **34**(3), pp. 213–221.
- [137] Butt, H., Cappella, B., and Kappell, M., 2005, "Force Measurements With the Atomic Force Microscope: Technique, Interpretation and Applications," *Surf. Sci. Rep.*, **59**, pp. 1–152.
- [138] Xu, Z., Kim, K., Zou, Q., and Shriotrya, P., 2008, "Broadband Measurement of Rate-Dependent Viscoelasticity at Nanoscale Using Scanning Probe Microscope: Poly(Dimethylsiloxane) Example," *Appl. Phys. Lett.*, **93**(13), p. 133103.
- [139] Perez, H., and Devasia, S., 2003, "Optimal Output Transitions for Linear Systems," *Automatica*, **39**(2), pp. 181–192.
- [140] Iamratanakul, D., and Devasia, S., 2009, "Minimum-Time/Energy, Output Transitions for Dual-Stage Systems," *ASME J. Dyn. Syst., Meas., Control*, **131**(2), p. 024503.
- [141] Lehenkari, P. P., Charras, G. T., Nykanen, A., and Horton, M. A., 2000, "Adapting Atomic Force Microscopy for Cell Biology," *Ultramicroscopy*, **82**, pp. 289–295.
- [142] Abraham, V. C., Krishnamurthi, V., Taylor, D. L., and Lanni, F., 1999, "The Actin-Based Nanomachine at the Leading Edge of Migrating Cells," *Biophys. J.*, **77**(3), pp. 1721–1732.
- [143] Small, J. V., Stradal, T., Vignal, E., and Rotter, K., 2002, "The Lamellipodium: Where Motility Begins," *Trends Cell Biol.*, **12**(3), pp. 112–120.
- [144] Mathur, A. B., Truskey, G. A., and Reichert, W. M., 2000, "Atomic Force and Total Internal Reflection Fluorescence Microscopy for the Study of Force Transduction in Endothelial Cells," *Biophys. J.*, **78**, pp. 1725–1735.
- [145] Grimellec, C. L., Lesniewska, E., Giocondi, M.-C., Finot, E., Vie, V., and Goudonnet, J.-P., 1998, "Imaging of the Surface of Living Cells by Low-Force Contact-Mode Atomic Force Microscopy," *Biophys. J.*, **75**, pp. 695–703.
- [146] Prater, C. B., Wilson, M. R., Garnaes, J., Massie, J., Elings, V. B., and Hansma, P. K., 1991, "Atomic Force Microscopy of Biological Samples at Low Temperature," *J. Vac. Sci. Technol. B*, **9**(2), pp. 989–991.
- [147] Schitter, G., Allgower, F., and Stemmer, A., 2004, "A New Control Strategy

- for High-Speed Atomic Force Microscopy,” *Nanotechnology*, **15**, pp. 108–114.
- [148] Tien, S., July 2007, “High-Speed Nano-Precision Positioning: Theory and Application to AFM Imaging of Soft Samples,” Ph.D. thesis, University of Washington, Seattle, WA.
- [149] Tien, S., and Devasia, S., 2009, “Rapid AFM Imaging of Large Soft Samples in Liquid With Small Forces,” *Asian J. Control*, **11**(2), pp. 154–165.
- [150] Fraden, J., 1993, *AIP Handbook of Modern Sensors: Physics Designs and Applications*, American Institute of Physics, New York.
- [151] Lapshin, R. V., 1998, “Automatic Lateral Calibration of Tunneling Microscope Scanners,” *Rev. Sci. Instrum.*, **69**(9), pp. 3268–3276.
- [152] Lapshin, R. V., 2004, “Feature-Oriented Scanning Methodology for Probe Microscopy and Nanotechnology,” *Nanotechnology*, **15**, pp. 1135–1151.
- [153] Cunningham, M., Jenkins, D., Clegg, W., and Bakush, M., 1995, “Active Vibration Control and Actuation of a Small Cantilever for Applications in Scanning Probe Instruments,” *Sens. Actuators, A*, **50**(1–2), pp. 147–150.